



The Core Population and Kinematics of a Massive Clump at Early Stages: An Atacama Large Millimeter/submillimeter Array View

Elena Redaelli¹ , Stefano Bovino^{2,3} , Patricio Sanhueza^{4,5} , Kaho Morii^{4,6} , Giovanni Sabatini³ , Paola Caselli¹ ,
Andrea Giannetti⁷, and Shanghuo Li⁸

¹ Centre for Astrochemical Studies, Max-Planck-Institut für extraterrestrische Physik, Gießenbachstraße 1, D-085748 Garching bei München, Germany
eredaelli@mpe.mpg.de

² Departamento de Astronomía, Facultad Ciencias Físicas y Matemáticas, Universidad de Concepción, Av. Esteban Iturra s/n Barrio Universitario, Casilla 160, Concepción, Chile

³ INAF—Istituto di Radioastronomia—Italian node of the ALMA Regional Centre (It-ARC), Via Gobetti 101, I-40129 Bologna, Italy

⁴ National Astronomical Observatory of Japan, National Institutes of Natural Sciences, 2-21-1 Osawa, Mitaka, Tokyo 181-8588, Japan

⁵ Department of Astronomical Science, The Graduate University for Advanced Studies, SOKENDAI, 2-21-1 Osawa, Mitaka, Tokyo 181-8588, Japan

⁶ Department of Astronomy, Graduate School of Science, The University of Tokyo, 7-3-1 Hongo, Bunkyo-ku, Tokyo 113-0033, Japan

⁷ INAF—Istituto di Radioastronomia, Via P. Gobetti 101, I-40129 Bologna, Italy

⁸ Korea Astronomy and Space Science Institute, 776 Daedeokdae-ro, Yuseong-gu, Daejeon 34055, Republic of Korea

Received 2022 May 27; revised 2022 July 11; accepted 2022 July 29; published 2022 September 12

Abstract

High-mass star formation theories make distinct predictions on the properties of the prestellar seeds of high-mass stars. Observations of the early stages of high-mass star formation can provide crucial constraints, but they are challenging and scarce. We investigate the properties of the prestellar core population embedded in the high-mass clump AGAL014.492-00.139, and we study the kinematics at the clump and clump-to-core scales. We have analyzed an extensive data set acquired with the Atacama Large Millimeter/submillimeter Array interferometer. Applying a dendrogram analysis to the Band 7 $\text{o-H}_2\text{D}^+$ data, we identified 22 cores. We fitted their average spectra in local thermodynamic equilibrium conditions, and we analyzed their continuum emission at 0.8 mm. The cores have transonic to mildly supersonic turbulence levels and appear to be mostly low-mass, with $M_{\text{core}} < 30 M_{\odot}$. Furthermore, we have analyzed Band 3 observations of the N_2H^+ (1–0) transition, which traces the large-scale gas kinematics. Using a friend-of-friend algorithm, we identify four main velocity coherent structures, all of which are associated with prestellar and protostellar cores. One of them presents a filament-like structure, and our observations could be consistent with mass accretion toward one of the protostars. In this case, we estimate a mass accretion rate of $\dot{M}_{\text{acc}} \approx 2 \times 10^{-4} M_{\odot} \text{ yr}^{-1}$. Our results support a clump-fed accretion scenario in the target source. The cores in the prestellar stage are essentially low-mass, and they appear to be subvirial and gravitationally bound, unless further support is available, for instance, due to magnetic fields.

Unified Astronomy Thesaurus concepts: [Star formation \(1569\)](#); [Massive stars \(732\)](#); [Interferometry \(808\)](#); [Astrochemistry \(75\)](#); [Star forming regions \(1565\)](#); [Interstellar line emission \(844\)](#)

Supporting material: interactive figure

1. Introduction

High-mass stars dominate the energetics of the interstellar medium (ISM), mainly due to feedback during their whole life cycle. Despite their importance, however, their formation process is significantly less known than for their low-mass counterparts. From a theoretical point of view, two main families of models have been developed. The core-accretion (or core-fed) model is a scaled-up version with respect to the low-mass process (McKee & Tan 2003). It predicts the existence of high-mass prestellar cores (HMPCs; M_{core} = several tens of solar masses), which are virialized either due to turbulence or to the contribution of magnetic pressure, that collapse as a whole (Tan et al. 2013, 2014). In the clump-fed or competitive accretion scenarios, instead, early fragmentation in high-mass clumps leads to the formation of essentially low-mass cores, which keep accreting mass from the dense surrounding environment also during the initial protostellar stages

(Bonnell et al. 2001; Bonnell & Bate 2006; Smith et al. 2009). In order to distinguish among the existing theories, observational constraints on the properties of the initial stages of high-mass star formation are needed, in particular in terms of the core masses and properties of accretion.

These observations are however challenging, as high-mass stars are intrinsically rarer and on average more distant than low-mass ones. The birthplace of high-mass stars is to be found in the heavily obscured environments of infrared dark clouds (IRDCs; Rathborne et al. 2006). In particular, IRDCs that are dark at 24 and 70 μm are supposed to host the earliest evolutionary stages of high-mass star formation (Sanhueza et al. 2013; Tan et al. 2013; Guzmán et al. 2015). Several studies have hence targeted IRDCs with interferometric facilities, such as the Atacama Large Millimeter/submillimeter Array (ALMA; as done by Zhang et al. 2015; Ohashi et al. 2016; Contreras et al. 2018; Sanhueza et al. 2019; Svoboda et al. 2019; Morii et al. 2021), or the Submillimeter Array (SMA; see, e.g., Sanhueza et al. 2017; Li et al. 2019; Pillai et al. 2019). Multiple works unveiled that the lack of emission at mid-infrared wavelengths as seen with single-dish facilities (e.g., the Spitzer Space Telescope) does not guarantee a complete lack of star formation activity, due to the high



Original content from this work may be used under the terms of the [Creative Commons Attribution 4.0 licence](#). Any further distribution of this work must maintain attribution to the author(s) and the title of the work, journal citation and DOI.

extinction that characterizes high-mass star-forming regions (see, e.g., Tan et al. 2016; Pillai et al. 2019; Li et al. 2020; Morii et al. 2021; Tafuya et al. 2021).

In this context, the ALMA Survey of 70 μm dark High-mass clumps in Early Stages survey (ASHES; Sanhueza et al. 2019) targeted 12 IRDCs with ALMA Band 6 observations. In the first paper of the series, the authors studied the clump fragmentation using the continuum emission at 1.3 mm, identifying ≈ 300 cores, none of which appear to be more massive than $30 M_{\odot}$. Continuum emission together with spectral line observations have the potential to provide a more complete picture of star-forming regions, in particular in terms of evolutionary stage assessment. For instance, outflow tracers (e.g., CO, SiO), or so-called warm transitions, which have high upper-level energies ($E_u > 20\text{--}30$ K), can be used to identify signs of protostellar activity, such as outflow emission or gas heating (see, e.g., Sanhueza et al. 2012; Li et al. 2020).

In the hunt for HMPCs, it is crucial to find a good and unambiguous tracer of the prestellar phases. Deuterated species appear to be promising to this aim. At low temperatures ($T < 20$ K) and high densities ($n \gtrsim 10^5 \text{ cm}^{-3}$) found in prestellar gas, most C- and O-bearing species are frozen out onto dust grains (Caselli et al. 1999; Bacmann et al. 2002). This contributes to increasing the abundance of H_2D^+ , the precursor of deuterated species in the gas phase, as this molecule is predominantly destroyed by reaction with CO (e.g., Ceccarelli et al. 2014, and references therein). This results in a boost of deuteration, and deuterated molecules can therefore be good probes of cold and dense gas.

Redaelli et al. (2021) reported the first $\text{o-H}_2\text{D}^+$ observations with ALMA in high-mass star-forming regions and showed that this molecule is a good probe of prestellar conditions. The $\text{o-H}_2\text{D}^+(1_{1,0}\text{--}1_{1,1})$ line was detected toward two intermediate-mass clumps (AG351 and AG354), at a spatial resolution of ≈ 1500 au. The authors identified 16 cores in total and estimated their masses from the continuum emission at 0.8 mm. At $T_{\text{dust}} = 10$ K, all cores are less massive than $10 M_{\odot}$, and the majority are subvirial, assuming negligible contribution to the stability from magnetic fields.

Molecular lines yield information also on the gas kinematics, which is of great importance when trying to investigate the accretion processes in high-mass clumps. Among the different tracers used, two important ones are ammonia (see, e.g., Lu et al. 2018; Williams et al. 2018; Sokolov et al. 2019) and N_2H^+ (Henshaw et al. 2014; Chen et al. 2019). The kinematics of high-mass star-forming regions can be studied by means of algorithms dedicated to identifying the hierarchy in their filamentary structures, as done, for instance, by Peretto et al. (2014), Chen et al. (2019), Henshaw et al. (2019), and Wang et al. (2020). Many of these works report the detection of velocity gradients usually interpreted as gas motions, linked to accretion flows toward cores or hubs (see, e.g., Hacar et al. 2022, and references therein).

The 70 μm dark clump AGAL014.492-00.139 (hereafter AG14) has an estimated mass of $5200 M_{\odot}$, and it is located at a distance of 3.9 kpc (Sanhueza et al. 2019). It belongs to the ATLASGAL TOP100 sample (Giannetti et al. 2014; König et al. 2017), a statistically significant sample of high-mass clumps at different evolutionary stages in the inner Galaxy. AG14 was also included among the targets of the ASHES project: Sanhueza et al. (2019) identified 37 cores in continuum, 25 of which are associated with warm lines or outflow emission. This point was investigated further by Li et al. (2020), who used CO and SiO observations with ALMA,

and found that six cores are associated with outflows. In particular, four present bipolar emission. Throughout this work, we will refer to these cores as protostellar (or protostars). More recently, Sakai et al. (2022) studied the emission of several deuterated molecules (N_2D^+ , DCO^+ , and DCN) found in ALMA Band 6.

In this work, we present an extensive ALMA data set on AG14, from 90 up to 370 GHz in Section 2, consisting of Band 3 data covering the N_2H^+ (1–0) line, Band 7 data of the $\text{o-H}_2\text{D}^+(1_{1,0}\text{--}1_{1,1})$ line, and Band 6 data of the N_2D^+ (3–2) transition (already published in Sakai et al. 2022). These different lines are used to trace distinct parts of the clump. H_2D^+ is mainly destroyed by reactions with CO, and it is hence sensitive to temperature rising beyond the CO desorption temperature (≈ 20 K). Furthermore, its $\text{o-H}_2\text{D}^+(1_{1,0}\text{--}1_{1,1})$ transition has a critical density of $n_c \approx 10^5 \text{ cm}^{-3}$ (Hugo et al. 2009); hence this line is an ideal tracer of cold and dense gas at the core scales. N_2H^+ is also a well-known high-density tracer. Its first rotational transition has a critical density of $6 \times 10^4 \text{ cm}^{-3}$, and it presents an isolated hyperfine component well separated from the others also in cases of large line widths ($\sigma_v \lesssim 2\text{--}4 \text{ km s}^{-1}$). This component is usually optically thin or only moderately optically thick (Sanhueza et al. 2012; Barnes et al. 2018; Fontani et al. 2021). In the intracloud gas in high-mass clumps, the N_2H^+ transition is excited over large scales. For all these reasons, N_2H^+ represents an ideal probe of the clump and clump-to-core kinematics. Finally, N_2D^+ is also a high-density tracer, but Giannetti et al. (2019) studied the correlation between the $\text{o-H}_2\text{D}^+(1_{1,0}\text{--}1_{1,1})$ and the N_2D^+ (3–2) transitions in three clumps embedded in the G351.77-0.51 complex, using single-dish data from APEX. The main result of those authors was an anticorrelation between the abundances of the two molecular species. This was explained as an evolutionary effect: in the prestellar phase, as time evolves, the abundance of $\text{o-H}_2\text{D}^+$ is expected to lower, mainly due the conversion to its doubly and triply deuterated forms (see also Sabatini et al. 2020). N_2D^+ instead forms later, and then its abundance keeps increasing, as it can be formed also from D_2H^+ and D_3^+ (see, e.g., the chemical model of Sipilä et al. 2013, 2015). These findings hinted to the possibility of using the abundance ratio between N_2D^+ and $\text{o-H}_2\text{D}^+$ as an evolutionary indicator, and we aim to investigate this point in AG14 with the available data.

The paper is organized as follows. The observations are presented in Section 2. In the analysis, we first investigate the core population embedded in the clump, using the $\text{o-H}_2\text{D}^+(1_{1,0}\text{--}1_{1,1})$ data (Section 3.1). We then present the clump-to-core kinematic properties in Section 3.2, based on the analysis of N_2H^+ (1–0) data. In Section 3.3 we analyze the correlation between the $\text{o-H}_2\text{D}^+$ and the N_2D^+ emission in the identified cores, and Section 4 contains a discussion and the concluding remarks of this work.

2. Observations

The observations used in this work are described in the following subsections, and the main technical details (e.g., angular resolution, sensitivity) are summarized in Table 1. If the data have already been published, we refer to the corresponding publication.

2.1. Band 7 Observations

The Band 7 data were observed during Cycle 6 as part of the ALMA project 2018.1.00331.S (PI: Bovino) in three runs

Table 1
Observational Parameters

Observation	Beam Size ^a	Spatial Res.	rms	Spectral Res.
Band 7				
Continuum 0.5 mm	0".66 × 0".50, PA = −73°.4	2600 au × 2000 au	0.8 mJy beam ^{−1}	...
o-H ₂ D ⁺ (1 _{1,0} –1 _{1,1})	0".67 × 0".50, PA = −73°.4	2600 au × 2000au	100 mK	0.20 km s ^{−1}
Band 6 ^b				
Continuum 1.34 mm	1".29 × 0".85, PA = 72°.5	5000 au × 3300au	0.17 mJy beam ^{−1}	...
N ₂ D ⁺ (3–2)	1".44 × 1".00, PA = 74°.8	5600 au × 3900 au	180 mK	0.17 km s ^{−1}
Band 3				
N ₂ H ⁺ (1–0)	2".86 × 1".61, PA = 74°.7	11200 au × 6200 au	110 mK	0.20 km s ^{−1}

Notes.

^a The beam size is shown as: major axis × minor axis, position angle (PA).

^b Data presented in Sanhueza et al. (2019) and Sakai et al. (2022).

(2018 November and 2019 March–April). The observations, performed as a single-pointing, made use of both the Main Array (12 m array, 45 antennas) and the 7 m array (12 antennas), with baselines ranging from 7 to 645 m. Quasars J1924–2914, J1911–2006, J1733–1304, and J1751+0939 were used as calibrators. The spectral setup comprises four spectral windows (SPWs). The first one, dedicated to the observation of the o-H₂D⁺(1_{1,0}–1_{1,1}) transition, is centered at frequency $\nu_{\text{rest}} = 372421.3558$ MHz (Jusko et al. 2017) and has a resolution of 244 kHz (corresponding to 0.20 km s^{−1} at 372 GHz) and a total bandwidth of 500 MHz. The second SPW is dedicated to the continuum, with a total bandwidth of 1.85 GHz around a frequency of 371 GHz.

At these frequencies, and with the used configuration, the maximum recoverable scale is $\theta_{\text{MRS}} \approx 20''$, the primary beams of the main array and of ACA are 17'' and 30'', respectively, and the angular resolution is $\approx 0''.6$ (corresponding to ≈ 2300 au at the distance of 3.9 kpc). The total observing times were 6.0 hr (7 m array) and 2.5 hr (12 m array). During the observations, the precipitable water vapor was typically 0.4 mm < PWV < 0.6 mm. The average system temperature values are found in the range 300–400 K for the SPW containing the o-H₂D⁺(1_{1,0}–1_{1,1}) line. The data were calibrated by the standard pipeline (CASA, version 5.4; McMullin et al. 2007). From a first inspection of the dirty maps, the emission both in the continuum and in lines appears to be very extended in the whole field of view (FoV). We therefore applied a modified weight of 2.4 to the ACA observations, similarly to what was done in Redaelli et al. (2021). After a few tests, this choice appeared to be the ideal compromise to maximize the recovery of the large-scale flux, without downgrading too much the final angular resolution.

We imaged the data using the `tclean` task of the software CASA (version 5.6), in interactive mode. We used the natural weighting and the multiscale deconvolver algorithm (Cornwell 2008; scales: 0, 5, 15). In order to avoid oversampling, both the continuum and the line images were regridded in order to ensure 3 pixels per beam minor axis, in agreement with the Nyquist theorem. Table 1 summarizes the achieved sensitivities and resolutions. The molecular line data have been converted into the brightness temperature T_b scale,

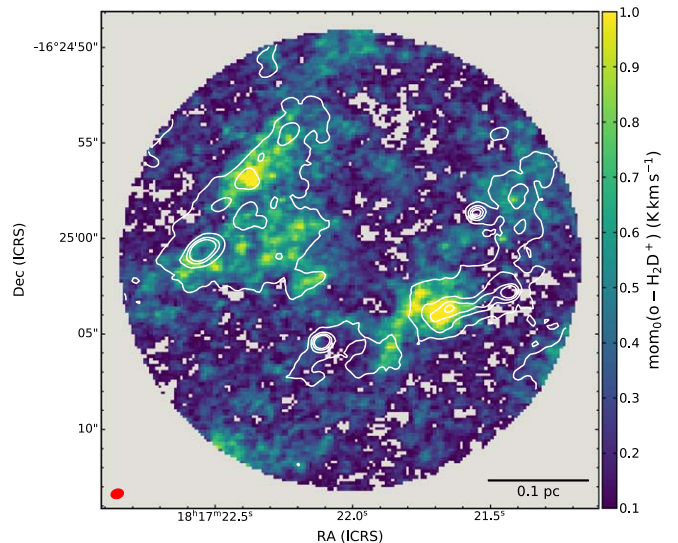


Figure 1. The color scale shows the integrated intensity of the o-H₂D⁺(1_{1,0}–1_{1,1}) line, where pixels below the 3 σ level have been masked. The mean uncertainty on the map is $1\sigma = 60$ mK km s^{−1}. The contours show the continuum emission at levels from 2 to 11 σ , in steps of 3 σ . Both continuum and line data are shown prior to primary-beam correction. The beam size and scale bar are indicated in the bottom left and right corners, respectively.

using the gain G computed as:

$$G = 1.222 \times 10^6 \frac{1}{\nu^2 \theta_{\text{min}} \theta_{\text{maj}}} = 26 \text{ mK}/(\text{mJy beam}^{-1}), \quad (1)$$

where ν is the frequency in GHz, and $\theta_{\text{min/maj}}$ are the beam sizes along the minor and major axes, respectively, expressed in arcsec.

Figure 1 shows the integrated intensity map of the o-H₂D⁺ line, computed in the velocity range 36–43 km s^{−1}, masking channels with a signal lower than 1 σ . The contours show the distribution of the continuum emission at 0.8 mm. Similarly to what has been noticed in Redaelli et al. (2021) in two different sources, the morphology of the continuum and of the line emission are in general different. Several bright peaks identified in dust thermal emission lack a counterpart in o-H₂D⁺ emission above the 3 σ level.

2.2. Band 6 Observations

The Band 6 data of the continuum emission and of the N_2D^+ (3–2) line at $\nu_{\text{rest}} = 231321.8283 \text{ MHz}$ ⁹ have been published by Sanhueza et al. (2019) and Sakai et al. (2022), respectively, and we refer to those papers for a complete description of the observations and of the data reduction. Briefly, the data were observed in Cycle 3 (Project ID: 2015.1.01539.S; PI: Sanhueza), with the 12 m array, the 7 m array (baselines ranging from 8 to 330 m), and the Total Power (the latter for spectral lines only). The data were acquired as mosaics, consisting of 10 pointings for the 12 m array and 3 for the 7 m array.

The spectral window containing the N_2D^+ line was imaged using the automatic clean script YCLEAN (Contreras et al. 2018), which uses natural weighting and multiscale deconvolver (scales: 0, 3, 10, 30). The CASA version 5.4 was used for the imaging. To allow for a better comparison with the $\text{o-H}_2\text{D}^+(1_{1,0}-1_{1,1})$ data (see Section 3.3), we have excluded the Total Power data for this analysis, and the maximum recoverable scale is $\theta_{\text{MRS}} = 35''$. The final angular resolution of the 12m+7 m combined data cube is $\approx 1''.0 \times 1''.4$, and the spectral resolution is 0.17 km s^{-1} . The data were converted from the flux scale to temperature scale through the gain $G = 15 \text{ mK}/(\text{mJy beam}^{-1})$, computed with Equation (1).

2.3. Band 3 Observations

The Band 3 data were collected as part of project 2018.1.00299.S (PI: Contreras), during Cycle 6. The data consist of 12 m array observations (performed in December 2018 and April 2019), 7 m array observations (performed in 2019 January), and Total Power (2019 April), with baseline ranging from 9.0 to 500 m. The average precipitable water vapor was in the range $4.6 \text{ mm} < \text{PWV} < 6 \text{ mm}$. Quasars J2000–1748, J1517–2422, and J1832–2039 were used as calibrators for the 12 m array data, while J1751+0939, J2056–4714, and J1911–2006 were used during the 7 m array observations.

In this paper, we focus on the N_2H^+ (1–0) transition at 93.174 GHz, which was targeted by a dedicated SPW with a spectral resolution of 61 kHz, corresponding to a velocity resolution of 0.20 km s^{-1} at the N_2H^+ frequency. The primary-beam size at the N_2H^+ frequency is $\approx 60''$ for the 12 m array, and $\approx 110''$ for the 7 m array. The line was imaged with Briggs weighting (robust=0.5) and multiscale deconvolver, using the `tclean` task of the software CASA (version 5.7). The scales used were 0, 5, 15, 25 times the pixel size ($0''.4$, corresponding to 1/4 of the beam minor axis, in agreement with the Nyquist sampling). The final beam size of the composite data cube (12m+7m+TP arrays), after primary-beam correction, is $2''.9 \times 1''.6$. The fluxes were converted in temperature scale using Equation (1), obtaining a gain of $G = 30 \text{ mK}/(\text{mJy beam}^{-1})$. The maximum recoverable scale considering the 12 and 7 m array configuration is $\theta_{\text{MRS}} = 85''$, but the Total Power observations further increase it.

3. Analysis

3.1. The Prestellar Core Population

The $\text{o-H}_2\text{D}^+(1_{1,0}-1_{1,1})$ emission traces cold and dense gas. In this section, we describe the analysis of the Band 7 data aimed to identify the population of prestellar cores in the clump and to study their properties.

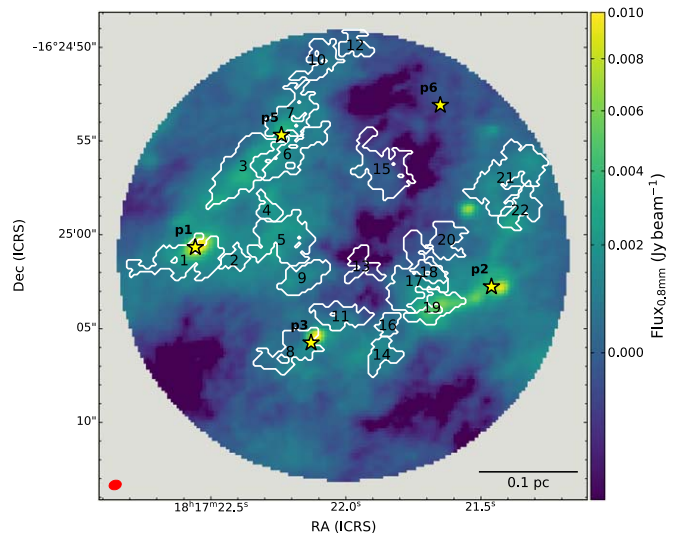


Figure 2. The cores identified in $\text{o-H}_2\text{D}^+$ by SCIMES are shown as white contours, on top of the continuum emission. They are labeled in order of decreasing right-ascension. The star symbols show the position of the protostellar cores identified by Li et al. (2020), labeled in bold face. The beam size and scale bar are indicated in the bottom left and right corners, respectively.

3.1.1. Prestellar Cores Identification

Our aim is to use the $\text{o-H}_2\text{D}^+(1_{1,0}-1_{1,1})$ data to identify structures (cores) that are in the early, prestellar stage. Similarly to what has been done in Redaelli et al. (2021), we use SCIMES (Colombo et al. 2015), which is based on the dendrogram algorithm (Rosolowsky et al. 2008) and analyzes data in the three-dimensional, position–position–velocity (ppv) space.

The first key step of SCIMES is the *dilmasking* masking technique, which maximizes the information recoverable in low signal-to-noise ratio (S/N) data (see Rosolowsky & Leroy 2006). The code identifies regions where the S/N is higher than a given threshold (S/N_{lim}) but contain emission peaks brighter than a second threshold (S/N_{peak}). After a few tests, we set $S/N_{\text{peak}} = 2$, and $S/N_{\text{lim}} = 1.5$, consistent with our choice in Redaelli et al. (2021), which maximizes the signal recovery. Another key parameter to build the dendrogram is the minimum height (in flux/brightness) that a structure must have to be cataloged as an independent leaf (Δ_{min}). We set the minimum height of an identified structure to $\Delta_{\text{min}} = 2.8 \times \text{rms}$ ¹⁰, where $\text{rms} = 100 \text{ mK}$ (this is the value obtained on the data cube before primary-beam correction, as SCIMES requires data with constant noise). We set the minimum number of channels that a leaf must span to $N_{\text{chan}}^{\text{min}} = 2$, and we mask structures smaller than 3 times the beam area. With these input parameters, we find 22 prestellar cores, shown in Figure 2. Some of them appear to overlap in projection on the plane of the sky. This is due to the fact that SCIMES works in the ppv space, and it is therefore able to identify distinct velocity components as belonging to different structures. We report in Table 2 the positions and sizes, expressed in terms of the effective radius, of the whole sample of cores.

Figure 2 confirms the fact that continuum and $\text{o-H}_2\text{D}^+$ emission do not perfectly correlate, as also seen in Figure 1. The positions of the protostellar candidates found by Li et al. (2020), also shown in

⁹ According to the Cologne Database for Molecular Spectroscopy (CDMS) available at <https://cdms.astro.uni-koeln.de/>.

¹⁰ Values tested in the range $\Delta_{\text{min}} = (2.5 - 3.5) \times \text{rms}$ lead to variation in only 18% of the identified structures. Using $\Delta_{\text{min}}/\text{rms} = 2.8$, instead of 3.0, allows the cores 21 and 22 to be separated, instead of merging in a single structure significantly larger than any other identified.

Table 2
Core Properties and Best-fit Results Obtained by Fitting their Average Spectra with MCWEEDS

Core id	Position		R_{eff}^a 10^3 au	rms K	V_{lsr} km s^{-1}	σ_v km s^{-1}	N_{col} $\log_{10}(\text{cm}^{-2})$	\mathcal{M}^b	M_{vir}^b M_{\odot}
	R.A. (h:m:s.ss)	decl. (d:m:s.ss)							
1	18: 17: 22.59	-16: 25: 1.35	5.5	0.09	$38.26^{+0.06}_{-0.06}$	$0.38^{+0.07}_{-0.06}$	$13.20^{+0.06}_{-0.06}$	$1.84^{+0.42}_{-0.38}$	$4.8^{+1.7}_{-1.4}$
2	18: 17: 22.41	-16: 25: 01.36	2.4	0.07	$38.96^{+0.10}_{-0.11}$	$0.34^{+0.02}_{-0.02}$	$12.91^{+0.07}_{-0.07}$	$1.61^{+0.02}_{-0.02}$	$1.74^{+0.04}_{-0.04}$
3	18: 17: 22.38	-16: 24: 56.44	6.1	0.07	$40.33^{+0.04}_{-0.05}$	$0.40^{+0.02}_{-0.04}$	$13.27^{+0.04}_{-0.04}$	$2.01^{+0.11}_{-0.24}$	$6.1^{+0.6}_{-1.1}$
4	18: 17: 22.29	-16: 24: 58.68	2.5	0.07	$38.38^{+0.05}_{-0.05}$	$0.29^{+0.05}_{-0.05}$	$13.02^{+0.06}_{-0.06}$	$1.32^{+0.34}_{-0.32}$	$1.4^{+0.5}_{-0.4}$
5	18: 17: 22.24	-16: 25: 0.27	5.5	0.03	$38.43^{+0.04}_{-0.04}$	$0.40^{+0.04}_{-0.03}$	$13.04^{+0.03}_{-0.03}$	$2.00^{+0.22}_{-0.19}$	$5.5^{+1.0}_{-0.9}$
6	18: 17: 22.22	-16: 24: 55.66	5.1	0.04	$39.71^{+0.05}_{-0.05}$	$0.30^{+0.01}_{-0.01}$	$12.96^{+0.04}_{-0.04}$	$1.37^{+0.01}_{-0.01}$	$2.96^{+0.03}_{-0.03}$
7	18: 17: 22.21	-16: 24: 53.65	4.5	0.06	$40.42^{+0.04}_{-0.04}$	$0.36^{+0.04}_{-0.03}$	$13.16^{+0.04}_{-0.04}$	$1.74^{+0.23}_{-0.19}$	$3.6^{+0.7}_{-0.5}$
8	18: 17: 22.21	-16: 25: 6.23	4.5	0.06	$41.01^{+0.12}_{-0.13}$	$0.42^{+0.09}_{-0.09}$	$12.72^{+0.11}_{-0.10}$	$2.08^{+0.50}_{-0.52}$	$4.8^{+2.1}_{-1.7}$
9	18: 17: 22.16	-16: 25: 2.31	3.9	0.04	$39.23^{+0.03}_{-0.03}$	$0.30^{+0.03}_{-0.03}$	$12.96^{+0.04}_{-0.04}$	$1.38^{+0.20}_{-0.20}$	$2.3^{+0.4}_{-0.4}$
10	18: 17: 22.10	-16: 24: 50.74	3.7	0.21	$40.43^{+0.11}_{-0.12}$	$0.33^{+0.10}_{-0.09}$	$13.26^{+0.11}_{-0.11}$	$1.58^{+0.59}_{-0.55}$	$2.6^{+1.5}_{-1.1}$
11	18: 17: 22.02	-16: 25: 4.36	3.9	0.04	$41.21^{+0.06}_{-0.06}$	$0.33^{+0.01}_{-0.02}$	$12.76^{+0.05}_{-0.06}$	$1.60^{+0.04}_{-0.04}$	$2.7^{+0.1}_{-0.1}$
12	18: 17: 21.97	-16: 24: 49.84	2.9	0.33	$40.57^{+0.15}_{-0.14}$	$0.28^{+0.02}_{-0.05}$	$13.34^{+0.16}_{-0.16}$	$1.26^{+0.12}_{-0.12}$	$1.5^{+0.2}_{-0.2}$
13	18: 17: 21.94	-16: 25: 1.57	3.1	0.04	$38.86^{+0.05}_{-0.05}$	$0.21^{+0.08}_{-0.04}$	$12.50^{+0.08}_{-0.08}$	$0.83^{+0.29}_{-0.30}$	$1.0^{+0.3}_{-0.3}$
14	18: 17: 21.87	-16: 25: 6.43	3.2	0.07	$41.46^{+0.06}_{-0.05}$	$0.34^{+0.05}_{-0.05}$	$13.11^{+0.06}_{-0.06}$	$1.64^{+0.29}_{-0.28}$	$2.4^{+0.7}_{-0.6}$
15	18: 17: 21.86	-16: 24: 56.45	5.3	0.04	$39.55^{+0.04}_{-0.04}$	$0.22^{+0.03}_{-0.03}$	$12.76^{+0.06}_{-0.06}$	$0.91^{+0.21}_{-0.23}$	$1.9^{+0.4}_{-0.4}$
16	18: 17: 21.84	-16: 25: 4.75	2.4	0.08	$41.44^{+0.04}_{-0.04}$	$0.29^{+0.04}_{-0.04}$	$13.15^{+0.05}_{-0.05}$	$1.28^{+0.09}_{-0.18}$	$1.2^{+0.1}_{-0.2}$
17	18: 17: 21.75	-16: 25: 2.60	6.2	0.03	$39.28^{+0.03}_{-0.03}$	$0.24^{+0.03}_{-0.03}$	$12.77^{+0.04}_{-0.05}$	$1.02^{+0.19}_{-0.21}$	$2.5^{+0.5}_{-0.5}$
18	18: 17: 21.68	-16: 25: 1.99	2.7	0.06	$37.93^{+0.06}_{-0.06}$	$0.19^{+0.11}_{-0.06}$	$12.61^{+0.12}_{-0.12}$	$0.66^{+0.56}_{-0.49}$	$0.8^{+0.6}_{-0.3}$
19	18: 17: 21.67	-16: 25: 3.87	4.2	0.05	$41.34^{+0.02}_{-0.02}$	$0.27^{+0.02}_{-0.02}$	$13.20^{+0.03}_{-0.03}$	$1.25^{+0.13}_{-0.13}$	$2.2^{+0.3}_{-0.3}$
20	18: 17: 21.63	-16: 25: 0.29	3.7	0.06	$39.28^{+0.07}_{-0.07}$	$0.31^{+0.06}_{-0.06}$	$12.82^{+0.07}_{-0.08}$	$1.49^{+0.36}_{-0.34}$	$2.3^{+0.8}_{-0.7}$
21	18: 17: 21.40	-16: 24: 56.93	6.2	0.11	$40.25^{+0.04}_{-0.04}$	$0.29^{+0.03}_{-0.03}$	$13.35^{+0.05}_{-0.05}$	$1.35^{+0.20}_{-0.20}$	$3.5^{+0.7}_{-0.7}$
22	18: 17: 21.35	-16: 24: 58.56	3.6	0.14	$40.36^{+0.06}_{-0.06}$	$0.30^{+0.04}_{-0.05}$	$13.29^{+0.07}_{-0.08}$	$1.42^{+0.26}_{-0.28}$	$2.2^{+0.6}_{-0.5}$

Notes. The rms values are standard deviation over line-free channels. Uncertainties in V_{lsr} , σ_v , N_{col} , one-dimension turbulent Mach number, and virial mass are expressed as 95% high-probability-density (HPD) intervals.

^a The effective radius is the radius of a circular region with the same area of the core.

^b The one-dimensional turbulent Mach number and the virial masses are computed assuming $T_{\text{gas}} = 10 \text{ K}$.

Figure 2, are usually associated with peaks in the continuum (with the exception of the one in the northwest corner), and either not associated with, or found at the edges of, the H_2D^+ -identified cores. In Appendix A we present a more detailed study of the continuum cores.

3.1.2. Core Properties from $\text{o-H}_2\text{D}^+$ Fitting

We perform a spectral fit of the $\text{o-H}_2\text{D}^+(1_{1,0}-1_{1,1})$ in each core, in order to derive maps of the centroid velocity (V_{lsr}), line width (FWHM), and column density $N_{\text{col}}(\text{o-H}_2\text{D}^+)$. We use the parallelized version of the MCWEEDS code (Giannetti et al. 2017), which is based on the WEEDS package of GILDAS (Maret et al. 2011). WEEDS is able to produce synthetic spectra in LTE approximation based on a set of input parameters (FWHM, V_{lsr} , molecular column density, excitation temperature, and source size), assuming that the line profile is Gaussian. MCWEEDS, instead, provides the framework to optimize the search for the best-fit solution of the parameters.¹¹ The code analyzes the spectrum in each pixel with Bayesian statistical models implemented using PYMC (Patil et al. 2010). In particular, we use a Markov chain Monte Carlo (MCMC) algorithm to sample the parameter space, with uninformative flat priors over the models' free parameters. Similarly as in Redaelli et al. (2021), for each position the code performs 100,000 iterations, with a burn-in of 1000 steps. For the excitation temperature, we assume $T_{\text{ex}} = 10 \text{ K}$ (see, e.g., Caselli et al. 2008; Friesen et al. 2014; Redaelli et al. 2021). The initial guesses for the free parameters are selected individually for each core. MCWEEDS uses the line FWHM as a free parameter, but here we show

the velocity dispersion instead ($\sigma_v = \text{FWHM} / (2\sqrt{2 \ln(2)})$). Figure 3 shows the best-fit maps of the free parameters, obtained composing together those of the single cores. We show the best-fit parameter maps for each core individually in Appendix B.

The centroid velocity shows little gradient within each core. Excluding core 6 (one of the largest in terms of physical size) and core 12, the dispersion of V_{lsr} around the average is less than 0.20 km s^{-1} . However, a clear change in V_{lsr} of the order of $3-4 \text{ km s}^{-1}$ is visible at the clump level, in particular with changing decl. We can identify three separate groups: i) the southernmost cores have typical velocities of $>41 \text{ km s}^{-1}$; ii) the cores in the central part of the clump present lower velocities ($V_{\text{lsr}} < 40 \text{ km s}^{-1}$). Group 1 and 2 overlap in the west part of the clump (see, e.g., core 19, 17, and 18); iii) in the northern part of AG14 the cores have typical velocities of $40-40.5 \text{ km s}^{-1}$. The presence of these three subpopulations of cores, with distinct velocities, suggests that AG14 presents a complex kinematics, with several velocity components that spatially overlap (see also the average spectra in Figure 5). This is further investigated in Section 3.2.

To investigate the core properties in terms of velocity dispersion and column density, we present the density distributions of these two parameters in Figure 4 (green color scale) and compare them with the results for AG351 and AG354 obtained in Redaelli et al. (2021).¹² We highlight that AG351 and AG354 are at about half of the distance with respect to AG14. However, the Band 7 data (both continuum and lines) were

¹¹ The source size is selected to ensure that the beam filling factor is unity.

¹² Due to a typo in the code, the column density values of Redaelli et al. (2021) were overestimated by a factor of $\sqrt{\pi}$. This does not affect the trends found in the comparison between the sources. However, in order to compare the results in AG14 with the ones in the other two sources, we corrected the latter before producing the plot in Figure 4.

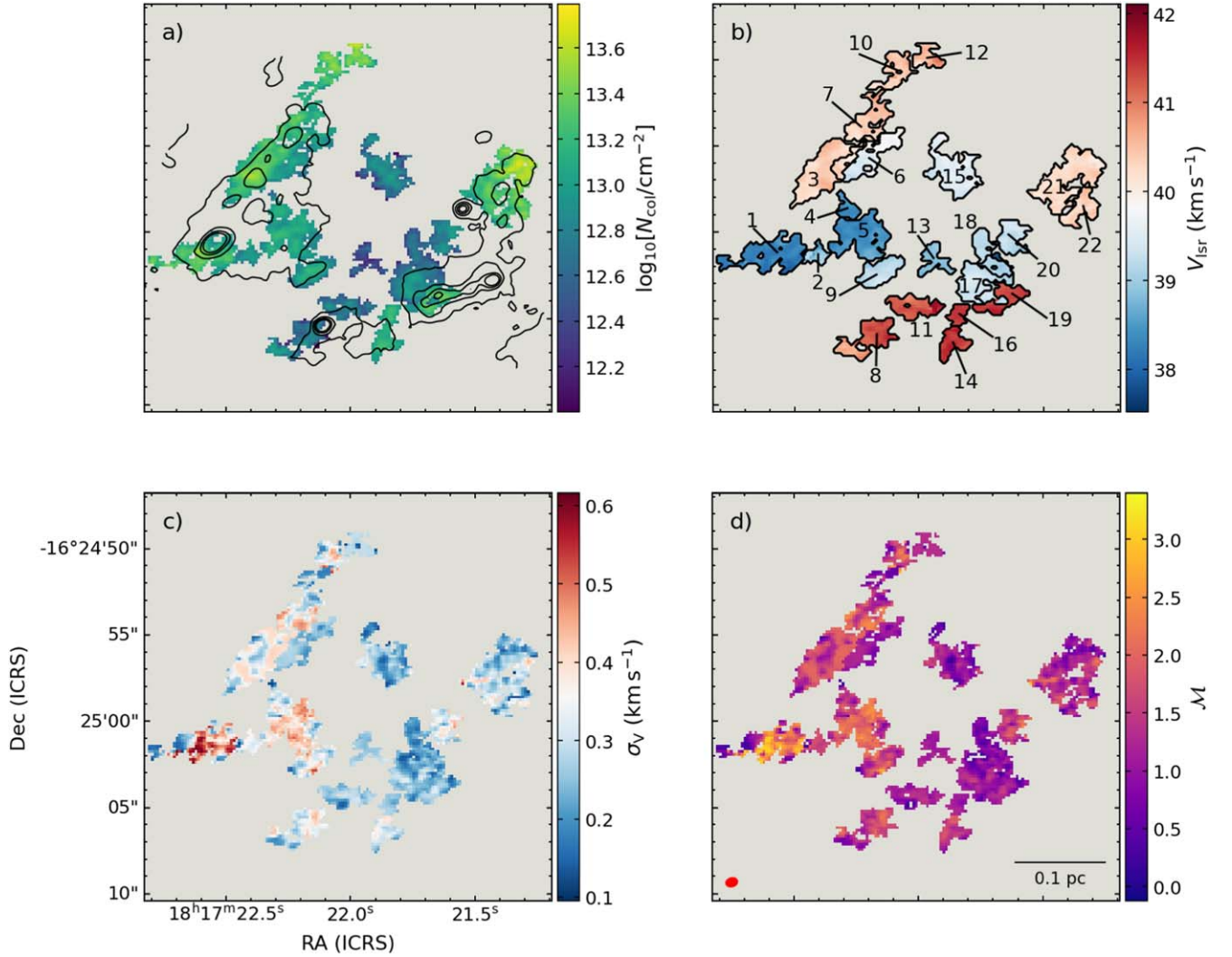


Figure 3. Composite maps obtained showing together the results of MCWEEDS fit on the $\text{o-H}_2\text{D}^+$ spectra for all the cores. Panel (a): molecular column density, with contours of the 0.8 mm continuum emission overlaid (levels from 2 to 11σ , in steps of 3σ); Panel (b): V_{lsr} map, with the $\text{o-H}_2\text{D}^+$ -identified cores shown in black contours, and numeric labels; Panel (c): velocity dispersion σ_v map; Panel (d): one-dimensional turbulent Mach number. Note that in case of core overlapping, the maps show the results of only one of them. For the complete sets of maps of each individual core we refer to Appendix B. The beam size and scale bar are indicated in the bottom left and right corners, respectively, of panel (d).

acquired with a higher angular resolution for AG14 ($\approx 0''.55$, to be compared with $\approx 0''.9$ for AG351 and AG354). Hence, the linear resolution of the data is only $\approx 25\%$ worse, allowing for a fair comparison. The average $\text{o-H}_2\text{D}^+$ column density in AG14 is $\langle N_{\text{col}} \rangle = 10^{13} \text{ cm}^{-2}$, which is consistent with the value obtained by Sabatini et al. (2020) with observations from the Atacama Pathfinder EXperiment (APEX), at a resolution ($17''$) comparable to the FoV of the ALMA data. The average velocity dispersion is $\langle \sigma_v \rangle = 0.30 \text{ km s}^{-1}$. AG14 presents on average higher column density values than AG351.

Furthermore, both clumps reported in Redaelli et al. (2021) showed very narrow lines, with a significant fraction on positions below both the isothermal sound speed at 10 K ($c_s = 0.19 \text{ km s}^{-1}$, assuming a gas mean molecular weight $\mu = 2.33$) and the thermal broadening of the $\text{o-H}_2\text{D}^+(1_{1,0}-1_{1,1})$ at 10 K ($\sigma_{v,\text{th}} = 0.14 \text{ km s}^{-1}$). On the contrary, in AG14 only 8% of the positions detected in $\text{o-H}_2\text{D}^+$ present $\sigma_v < c_s$ (to be compared with 36% and 23% in AG351 and AG354, respectively), and less than 1% are characterized by $\sigma_v < \sigma_{v,\text{th}}$ (17% and 7% in AG351 and AG354). The gas motions in AG14 hence appear to be less quiescent than those in AG351

and AG354. We highlight that the derived velocity dispersion values might be overestimated due to the limited spectral resolution of our observations. Lines narrower than $\text{FWHM} = 0.6 \text{ km s}^{-1}$ (corresponding to $\sigma_v = 0.25 \text{ km s}^{-1}$), in fact, are resolved by less than three channels. However, the spectral resolution is the same for all three clumps, and therefore this problem would not affect the comparison between the sources. In Appendix C we discuss also the line width overestimation due to opacity effect, which is found to be at most 15% and only in the densest parts of the AG14.

From the total velocity dispersion σ_v , the nonthermal contribution can be computed, under the assumption that the thermal and nonthermal contributions are independent, and thus they sum in quadrature (see, e.g., Myers et al. 1991):

$$\sigma_{v,\text{NT}} = \sqrt{\sigma_v^2 - \sigma_{v,\text{th}}^2} = \sqrt{\sigma_v^2 - \frac{k_B T_{\text{gas}}}{m_{\text{H}_2\text{D}^+}}}, \quad (2)$$

where $m_{\text{H}_2\text{D}^+}$ is the H_2D^+ molecular mass (in g, 4 a.m.u.), T_{gas} is the gas temperature (assumed to be 10 K), and k_B is the Boltzmann constant. The one-dimensional turbulent Mach

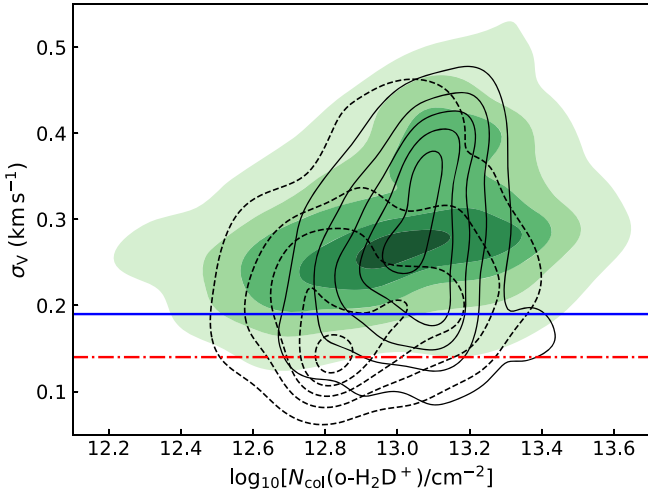


Figure 4. The green color scale shows the normalized kernel density distribution of σ_v and N_{col} in AG14, with the contour levels set on [0.1, 0.3, 0.5, 0.7, 0.9]. The same data are shown for AG351 with the dashed contours and for AG354 with solid contours (taken from Redaelli et al. 2021; the N_{col} values have been corrected by a factor $\sqrt{\pi}$; see text for details). The horizontal blue solid and red dashed-dotted lines represent the sound speed and the thermal broadening of $\text{o-H}_2\text{D}^+$, respectively, both at 10 K.

number is then $\mathcal{M} = \sigma_{v,\text{NT}}/c_s$. The bottom-right panel of Figure 3 shows the map of this parameter. In most of the cores, the turbulent motions are transonic or mildly supersonic ($\mathcal{M} = 1\text{--}2$). A few cores, however, present subsonic non-thermal line widths (e.g., cores n . 15, 17, 18, and 19).

3.1.3. Average Core Properties

An assessment of the dynamical state of each core can be obtained from the one-dimensional turbulent Mach number and the virial mass. These quantities are computed by fitting the averaged spectra within each core via MCWEEDS. The average spectra in each core, together with the obtained best-fit models, are shown in Figure 5, and the best-fit values are presented in Table 2. In Figure 5 we have highlighted with a blue asterisk those cores with significant overlap (at least 5% of their extension) with at least one other core. These cases present either multiple velocity components well separated in velocity (e.g., cores 17 and 18), or broad wings and shoulders (core 6). We however select the initial guesses for the fit of the average spectra from the results of the pixel-by-pixel fit of each core, and MCWEEDS is hence able to identify and fit the correct velocity component.

From the σ_v values derived by fitting the average spectra we computed the one-dimensional turbulent Mach number in each core, following the procedure described in Section 3.1.2. Furthermore, we derived the total velocity dispersion of the gas (σ_{dyn}) as:

$$\sigma_{\text{dyn}} = \sqrt{\sigma_{\text{NT}}^2 + c_s^2}, \quad (3)$$

from which we can derive the virial mass of the cores using the equation of Bertoldi & McKee (1992), under the assumption of uniform density (MacLaren et al. 1988):

$$M_{\text{vir}} = \frac{5R_{\text{core}}\sigma_{\text{dyn}}^2}{G} = 1200 \times \left(\frac{R_{\text{core}}}{\text{pc}}\right) \left(\frac{\sigma_{\text{dyn}}}{\text{km s}^{-1}}\right)^2 M_{\odot}, \quad (4)$$

where for the R_{core} values we have used the effective radii listed in Table 2. This definition of the virial mass ignores contributions from magnetic fields and external pressure.

The values of \mathcal{M} span the range 0.7–2.0, with an average of $\langle\sigma_{v,\text{NT}}/c_s\rangle = 1.4$. The turbulent motions in AG14 are transonic, or mildly supersonic. The $\sigma_{v,\text{NT}}/c_s$ values are significantly lower than the value reported by Sabatini et al. (2020) using APEX observations ($\sigma_{v,\text{NT}}/c_s = 5.4$), most likely because the unresolved single-dish spectrum overestimates the line width, due to the velocity gradient that the ALMA data unveil ($\approx 4 \text{ km s}^{-1}$) and the presence of several velocity components. The virial masses derived at 10 K are found within the range 0.8–6.1 M_{\odot} , with 50% of the cores presenting $M_{\text{vir}} < 2.4 M_{\odot}$. If the prestellar cores identified in $\text{o-H}_2\text{D}^+$ are virialized, they are essentially low-mass.

In the analysis of the $\text{o-H}_2\text{D}^+(1_{1,0}\text{--}1_{1,1})$ transition performed so far, we have assumed that the line opacity is low, and that the missing flux due to the filtering of the large-scale emission from the interferometer is negligible. We discuss these points in further detail in Appendix C.

3.1.4. Continuum Emission

Further information on the core properties comes from the analysis of the continuum emission. In particular, we can estimate the core total mass (M_{core}) using the equation:

$$M_{\text{core}} = f \frac{D^2 S_{\text{tot}}}{B_{\nu}(T_{\text{dust}}) \kappa_{\nu}}, \quad (5)$$

where f is the gas-to-dust ratio (assumed to be 100; Hildebrand 1983); D is the source’s distance; $B_{\nu}(T_{\text{dust}})$ is the Planck function at frequency $\nu = 371 \text{ GHz}$ and temperature T_{dust} ; S_{tot} is the 0.8 mm total flux integrated within the contours of the $\text{o-H}_2\text{D}^+$ -identified cores, and κ_{ν} is the dust opacity at the frequency of the observations. For the latter, we use the power-law expression:

$$\kappa_{\nu} = \kappa_0 \left(\frac{\nu}{\nu_0}\right)^{\beta} = 1.71 \text{ cm}^2 \text{ g}^{-1}, \quad (6)$$

in which we use $\beta = 1.5$ for the dust emissivity index (Mezger et al. 1990; Walker et al. 1990) and $\kappa_0 = 10 \text{ cm}^2 \text{ g}^{-1}$ for the dust opacity at the reference wavelength $\lambda_0 = 250 \mu\text{m}$ (Hildebrand 1983; Beckwith et al. 1990). Under the assumption of spherical symmetry and uniform gas distribution, we can evaluate the gas density as:

$$n(\text{H}_2) = \frac{3M_{\text{core}}}{4\pi R_{\text{eff}}^3 \mu_{\text{H}_2} m_{\text{H}}}, \quad (7)$$

where m_{H} and $\mu_{\text{H}_2} = 2.8$ are, respectively, the hydrogen mass and the gas mean molecular weight per hydrogen molecule (Kauffmann et al. 2008).

Equation (5) and, as a consequence, Equation (7) depend on the dust temperature. Under the hypothesis that the line is excited in LTE conditions (which holds for $n(\text{H}_2) \gtrsim 10^5 \text{ cm}^{-3}$; Hugo et al. 2009) and that the gas and dust are thermally coupled (which requires $n(\text{H}_2) \gtrsim 10^{4-5} \text{ cm}^{-3}$; Goldsmith 2001), we can assume that $T_{\text{dust}} = T_{\text{gas}} = T_{\text{ex}}(\text{o-H}_2\text{D}^+) = 10 \text{ K}$. However, in order to relax these assumptions and to take into consideration that locally the dust and gas temperatures could differ, we have computed the

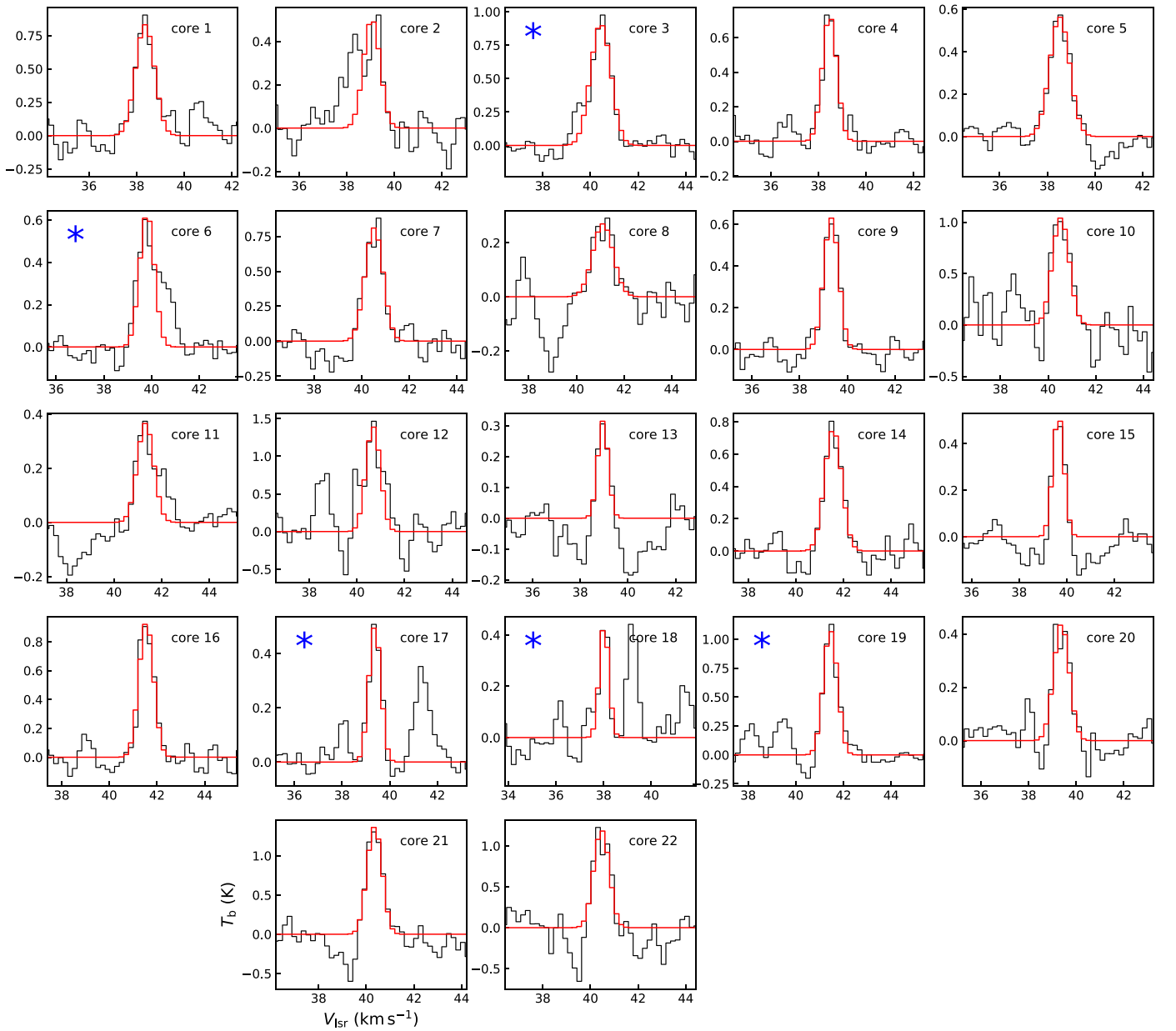


Figure 5. In black we show the average $\text{o-H}_2\text{D}^+(1_{1,0}-1_{1,1})$ spectra obtained in each core (labeled at the top-right corner of each panel). The red histogram shows the best-fit obtained with MCWEEDS. The corresponding best-fit parameters are recorded in Table 2. Cores that overlap by at least 5% of their extension with another core are marked with a blue asterisk in the top-left corner of the panel.

core masses and average densities at three temperatures, equal to 10, 15, and 20 K. The obtained values are summarized in Table 3. From this analysis, we exclude cores that are undetected in continuum, meaning that they lack of peak flux above the 3σ level. At 10 K, the point-like mass sensitivity of our observations is $0.6 M_\odot$ (3σ level). Due to the different morphology that the continuum and molecular line data present, as discussed in Section 3.1.1, eight cores are excluded.

Regarding uncertainties, we follow Sanhueza et al. (2017; see in particular their Section 5.6), and we assume a 23% uncertainty on the dust-to-mass-ratio, and 28% uncertainty on the dust opacity. Furthermore, we assume a 10% uncertainty on the source’s distance. Hence, the uncertainty on the mass and on the density values are 38%. In Equation (5), the total flux is computed integrating the continuum data within each core masks; in case of core overlap, naturally, this will cause an

overestimation of their masses. This problem is more severe with increasing overlap area. We have estimated the significance of this bias using the method presented by Li et al. (2020) to decompose the dust-estimated masses of cores when spectroscopic data are available, under the hypothesis that the molecular transition is a high-density tracer (i.e., it traces densities higher than the threshold for dust-gas coupling) and is optically thin. Under these assumptions, which are both reasonably valid for our $\text{o-H}_2\text{D}^+$ data, one can decompose the continuum flux into different cores according to the ratio of the line integrated intensity of each velocity component with respect to the total integrated intensity (computed over all the velocity components). We have performed this analysis for the five cores that overlap by more than 5% of their area (see also Figure 5). We find that on average their masses are overestimated by 23%, i.e., less than the uncertainties here

Table 3
Core Properties Derived from the Continuum Emission at 0.8 mm

Core id	M_{core}	$n(\text{H}_2)$	α_{vir}	M_{core}	$n(\text{H}_2)$	α_{vir}	M_{core}	$n(\text{H}_2)$	α_{vir}
	M_{\odot}	10^6cm^{-3}		M_{\odot}	10^6cm^{-3}		M_{\odot}	10^6cm^{-3}	
	10 K			15 K			20 K		
1	27 ± 10	4.9 ± 1.9	0.18 ± 0.08	13 ± 5	2.3 ± 0.9	0.40 ± 0.17	8 ± 3	1.4 ± 0.5	0.7 ± 0.3
2	1.9 ± 0.7	4.0 ± 1.5	0.9 ± 0.4	0.9 ± 0.3	1.8 ± 0.7	2.1 ± 0.9	0.5 ± 0.2	1.2 ± 0.4	3.6 ± 1.5
3	19 ± 7	2.5 ± 0.9	0.33 ± 0.14	9 ± 3	1.1 ± 0.4	0.8 ± 0.3	5 ± 2	0.7 ± 0.3	1.2 ± 0.5
4	2.2 ± 0.8	4.3 ± 1.6	0.6 ± 0.3	1.0 ± 0.4	2.0 ± 0.8	1.5 ± 0.6	0.6 ± 0.2	1.2 ± 0.5	2.5 ± 1.1
5	9 ± 3	1.5 ± 0.6	0.7 ± 0.3	3.9 ± 1.5	0.7 ± 0.3	1.5 ± 0.6	2.5 ± 0.9	0.4 ± 0.2	2.4 ± 1.0
6	10 ± 4	2.1 ± 0.8	0.31 ± 0.13	4.4 ± 1.7	1.0 ± 0.4	0.7 ± 0.3	2.8 ± 1.0	0.6 ± 0.2	1.2 ± 0.5
7	9 ± 4	3.1 ± 1.2	0.39 ± 0.17	4.3 ± 1.6	1.5 ± 0.6	0.9 ± 0.4	2.7 ± 1.0	0.9 ± 0.3	1.5 ± 0.6
8	6 ± 2	1.9 ± 0.7	0.8 ± 0.4	2.7 ± 1.0	0.9 ± 0.3	1.9 ± 0.8	1.7 ± 0.6	0.6 ± 0.2	3.1 ± 1.3
10	2.8 ± 1.1	1.6 ± 0.6	0.9 ± 0.4	1.3 ± 0.5	0.8 ± 0.3	2.2 ± 0.9	0.8 ± 0.3	0.5 ± 0.2	3.6 ± 1.6
17	8 ± 3	1.0 ± 0.4	0.32 ± 0.14	3.7 ± 1.4	0.5 ± 0.2	0.8 ± 0.3	2.3 ± 0.9	0.3 ± 0.1	1.3 ± 0.6
18	1.0 ± 0.4	1.6 ± 0.6	0.8 ± 0.3	0.5 ± 0.2	0.8 ± 0.3	1.9 ± 0.8	0.30 ± 0.11	0.5 ± 0.2	3.3 ± 1.4
19	13 ± 5	5 ± 2	0.16 ± 0.07	6 ± 2	2.5 ± 0.9	0.38 ± 0.16	3.9 ± 1.5	1.6 ± 0.6	0.6 ± 0.3
21	20 ± 7	2.4 ± 0.9	0.18 ± 0.08	9 ± 3	1.1 ± 0.4	0.42 ± 0.18	6 ± 2	0.7 ± 0.3	0.7 ± 0.3
22	8 ± 3	5.0 ± 1.9	0.28 ± 0.12	3.6 ± 1.4	2.3 ± 0.9	0.6 ± 0.3	2.3 ± 0.9	1.5 ± 0.6	1.1 ± 0.5

Note. The core masses, volume densities, and virial parameters are computed at three distinct temperatures: 10, 15, and 20 K. The uncertainty on the core masses and densities is 38%, while it is 43% on the virial parameter values.

considered. We conclude that this possible bias does not significantly affect our results.

Focusing on the gas density values, we note that also assuming a higher dust temperature of 20 K, all the cores have average densities higher than $3 \times 10^5 \text{cm}^{-3}$. This level is comparable to the critical density of the $\text{o-H}_2\text{D}^+(1_{1,0}-1_{1,1})$ line, corroborating the assumption both of LTE conditions for this transition, and of dust-gas coupling. Regarding the masses, all cores are less massive than $30 M_{\odot}$ at any temperature value considered here. This is consistent with what is found by Sanhueza et al. (2019), who identified cores (at any evolutionary stage) in continuum Band 6 data. We however highlight that the lack of Total Power observations in continuum can lead to partial filter-out of the large-scale emission, hence underestimating the mass values.¹³

In Table 3 we report also the virial parameter values ($\alpha_{\text{vir}} = M_{\text{vir}}/M_{\text{core}}$) at the three temperatures here considered. The uncertainty on α_{vir} takes the 38% uncertainty on the core masses and a further 20% error into account, which corresponds to the average uncertainty on the virial mass values. At low dust temperature ($T_{\text{dust}} = 10 \text{K}$), all cores present $\alpha_{\text{vir}} < 1.0$, suggesting that they are both subvirial and gravitationally bound. Also at $T_{\text{dust}} = 15 \text{K}$, we derived $0.3 \leq \alpha_{\text{vir}} \leq 2.2$, and all cores are gravitationally bound ($\alpha_{\text{vir}} < 2$) within uncertainties. The virial parameter increases with temperature, but still at $T_{\text{dust}} = 20 \text{K}$ 50% of the cores in the sample are subvirial within uncertainties. In particular, the most massive cores present the lowest α_{vir} values ($\alpha_{\text{vir}} \lesssim 0.3$ for $M_{\text{core}} \gtrsim 8 M_{\odot}$), in agreement with several observational results (see, e.g., Kauffmann et al. 2013). This suggests that the largest cores in the sample are not in equilibrium, unless other sources of pressure (e.g., magnetic fields) contribute to the virialization.

Singh et al. (2021) performed an extensive study regarding biases in the computation of the virial parameter that tend to lead to its underestimation. Those authors in particular

discussed the role of *i*) neglecting the gas bulk motions in the calculation of σ_{dyn} and of *ii*) the subtraction of the background emission. They found that when these aspects are taken into account, many cores that appeared to be subvirial become instead virialized or supervirial. However, our analysis intrinsically limits this problem. As σ_{dyn} is computed from averaged spectra in each core, bulk motions—if present—are already taken into account as they increase the velocity dispersion of the averaged signal. Furthermore, as noted also by Singh et al. (2021), interferometric observations naturally filter out the large-scale emission, hence performing an approximate background subtraction. We conclude that these effects are likely negligible in our results.

We now discuss the properties of the most massive cores identified. Core 1, with $M_{\text{core}} \approx 30 M_{\odot}$ at 10 K is the most massive core, and it is subvirial at any temperature value considered in this work. However, we have reasons to believe that this core is not in a prestellar stage. In fact, it overlaps with a continuum core associated with outflow emission and protostellar activity (see Appendix A). The continuum flux peak is found close to the edge of the core, suggesting that $\text{o-H}_2\text{D}^+$ is tracing the part of the envelope, which is still cold and dense enough to emit the $\text{o-H}_2\text{D}^+(1_{1,0}-1_{1,1})$ transition. A similar discussion could be made for core 3, which has $M_{\text{core}} = 20 M_{\odot}$ (at 10 K) and it is subvirial, and it lays in close proximity to protostar p5. Also core 21 has a similar mass, but unlike the other two, no protostellar core appears to be found in its surroundings. However, a significant continuum peak is found just outside its southeast edge. This peak is associated with the continuum-identified structure c8 (see Appendix A, where we speculated about the evolutionary stage of this core).

In Figure 6 we compare the masses and sizes of the identified cores in AG351, AG354, and AG14 (at $T_{\text{dust}} = 10 \text{K}$). Cores in AG14 appear to be on average larger and more massive than in the other two clumps, as expected by the availability of a larger mass reservoir, as AG14 is a factor of ≈ 30 more massive than the other two sources. In the figure, we also report several estimations of the threshold for high-mass star formation in the mass–size space. Krumholz & McKee (2008) derived analytically the

¹³ The integrated flux over the ALMA Band 7 FoV computed from the APEX 870 μm (from the ATLASGAL survey) is $\approx 2.5 \text{Jy}$, while the total integrated flux in the ALMA data is only 0.8 Jy, suggesting a significant loss of flux in the large-scale emission.

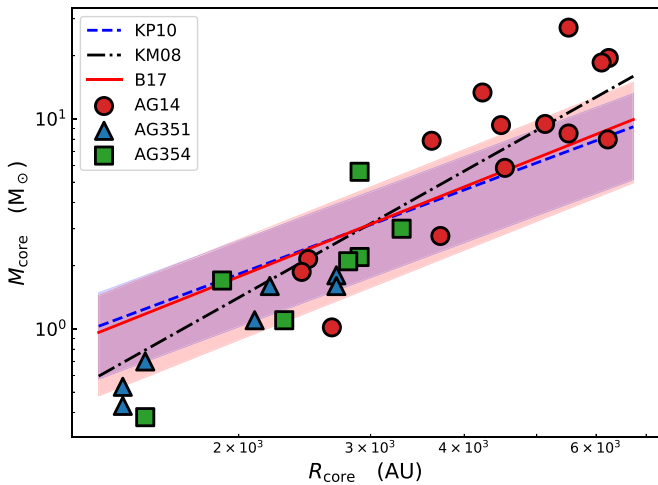


Figure 6. Core masses vs. sizes in AG351 (blue triangles), AG354 (green squares), and AG14 (red circles). The thresholds for high-mass star formation described by Krumholz & McKee (2008), Kauffmann & Pillai (2010), and Baldeschi et al. (2017) are shown with the dashed-dotted black curve, the dashed blue curve, and the solid red line, respectively. For the last two relations we also indicated uncertainties with shaded blue and red areas, which reflect differences in the dust opacity values used here and in those works. The uncertainties on M_{core} are 30% (AG351 and AG354) and 38% (AG14).

surface density limit of $\Sigma \approx 1 \text{ g cm}^{-2}$, which roughly translates into $M/M_{\odot} = 15 \times 10^3 (R/\text{pc})^2$. From observational data of several IRDCs, Kauffmann & Pillai (2010) derived the relation $M/M_{\odot} = 870 (R/\text{pc})^{1.33}$, while more recently Baldeschi et al. (2017) reported $M/M_{\odot} = 1282 (R/\text{pc})^{1.42}$, based on the analysis of clouds in the Herschel Gould Belt survey. The most massive cores in AG14 sit well above all the relations here studied, and have therefore the potential to form high-mass stars in the future. However, as their masses are $M_{\text{core}} \approx 10\text{--}30 M_{\odot}$, they still need to accrete significant mass from the surrounding environment, unless the star formation efficiency is locally high.

As previously noted, the angular resolutions of the observations of the three clumps are well matched to their distinct distances. However, the angular maximum recoverable scale is approximately the same for all the sources, which means that more large-scale flux is recovered in AG351 and AG354 with respect to AG14. This might affect the comparison between the core masses, which could be overestimated in AG351 and AG354 with respect to AG14. This however would not affect our conclusion that cores in the last clump are more massive than in the first two sources.

3.2. The Clump-to-core Scale Kinematics

The centroid velocity map obtained by fitting the $\text{o-H}_2\text{D}^+(1_{1,0}\text{--}1_{1,1})$ data, shown in Figure 3, suggests a complex kinematics of the source, as indicated by the presence of several velocity components at many positions. In order to investigate the kinematics of AG14 at the clump scale, we have used ALMA Band 3 observations of the $\text{N}_2\text{H}^+(1\text{--}0)$ transition. As illustrated in Section 1, this transition is better suited to trace the gas at larger scales than the $\text{o-H}_2\text{D}^+(1_{1,0}\text{--}1_{1,1})$ data. Furthermore, the Band 3 data have a spatial resolution of $11200 \text{ au} \times 6180 \text{ au}$ ($0.05 \text{ pc} \times 0.03 \text{ pc}$), and they were acquired including Total Power observations (not available in the Band 7 data set), which increases the sensitivity to the large-scale emission. These observations are therefore ideal to

probe the large-scale kinematics of the gas in which the cores identified in $\text{o-H}_2\text{D}^+$ are embedded.

We focused on the isolated hyperfine component $F_1 = 0\text{--}1$ of the $\text{N}_2\text{H}^+(1\text{--}0)$ transition, which is supposed to be optically thin or only moderately optically thick even at the high column densities found in high-mass star-forming regions (see, e.g., Sanhueza et al. 2012; Barnes et al. 2018; Fontani et al. 2021). The integrated intensity of this component is shown in the left panel of Figure 7, where we also overlap the contours of the $\text{o-H}_2\text{D}^+$ cores and the positions of the protostellar objects (star symbols). The FoV has been cut to the central $40'' \times 40''$, focusing on the map area also covered by the Band 7 data. The N_2H^+ emission is extended over almost the whole map coverage. The morphology appears to be filamentary, with several clumpy peaks of emission. Several of these peaks coincide with the position of protostellar candidates.

By a visual inspection of the data cube, it appears that three velocity components are present on a large extension of the source. We have hence proceeded with a three-components Gaussian fit using the PYSPECKIT package (Ginsburg & Mirocha 2011). The technical details of the fitting routine are described in Appendix D. Figure 8 shows the comparison of the spectra of $\text{o-H}_2\text{D}^+$ and N_2H^+ at the peak of the $\text{o-H}_2\text{D}^+$ integrated intensity, for each core identified in Section 3.1.1. The correspondence between the two species is remarkable. Every velocity components seen in $\text{o-H}_2\text{D}^+$ is associated also with a N_2H^+ component, while the opposite is not true. Furthermore, for corresponding components, $\text{o-H}_2\text{D}^+(1_{1,0}\text{--}1_{1,1})$ tends to present narrower line widths with respect to the N_2H^+ line. These findings suggest the following scenario: over the whole clump, at least three gas components (separated in velocity usually by $0.5\text{--}1.0 \text{ km s}^{-1}$) are visible, as traced by N_2H^+ , an abundant molecule that probes gas densities of $n \gtrsim 10^4 \text{ cm}^{-3}$. Within these large-scale structures, cores are formed, with significantly higher densities ($n > 10^5 \text{ cm}^{-3}$; see also Table 3). The gas within the cores is hence cold and dense, and it excites the $\text{o-H}_2\text{D}^+(1_{1,0}\text{--}1_{1,1})$ emission. Arising from a more quiescent medium, the $\text{o-H}_2\text{D}^+(1_{1,0}\text{--}1_{1,1})$ spectra are narrower than the N_2H^+ ones, which instead are associated with larger scale, more turbulent gas, as suggested by the broader line widths of this species.

The N_2H^+ data allow us to study not only the kinematics within the cores (better traced by the $\text{o-H}_2\text{D}^+$ data) but also that of the intraclump gas in which the cores are embedded, as we are able to link kinematically each core with one N_2H^+ component. In order to investigate the gas structure in the ppv space, we used the Agglomerative Clustering for ORganising Nested Structures (ACORNS; Henshaw et al. 2019). Similarly to SCIMES, ACORNS is a hierarchical clustering algorithm, which identifies structures and their hierarchical links in the ppv space. However, unlike SCIMES, ACORNS is designed to work on already decomposed data. In other words, instead of working on the observed data cubes, it operates on the fitting results of the multicomponent Gaussian fit described previously. The technical details about the ACORNS clustering are given in Appendix D. Using the terminology of Henshaw et al. (2019), ACORNS finds a forest of 18 trees in total, 4 of which contain $\approx 70\%$ of all data points and $\approx 80\%$ of the total flux. These trees present also the most complex hierarchical structures, containing each between two and seven leaves.

In Figure 9 we show a screenshot of the 3D ppv plot of the four main trees found by ACORNS, together with the positions

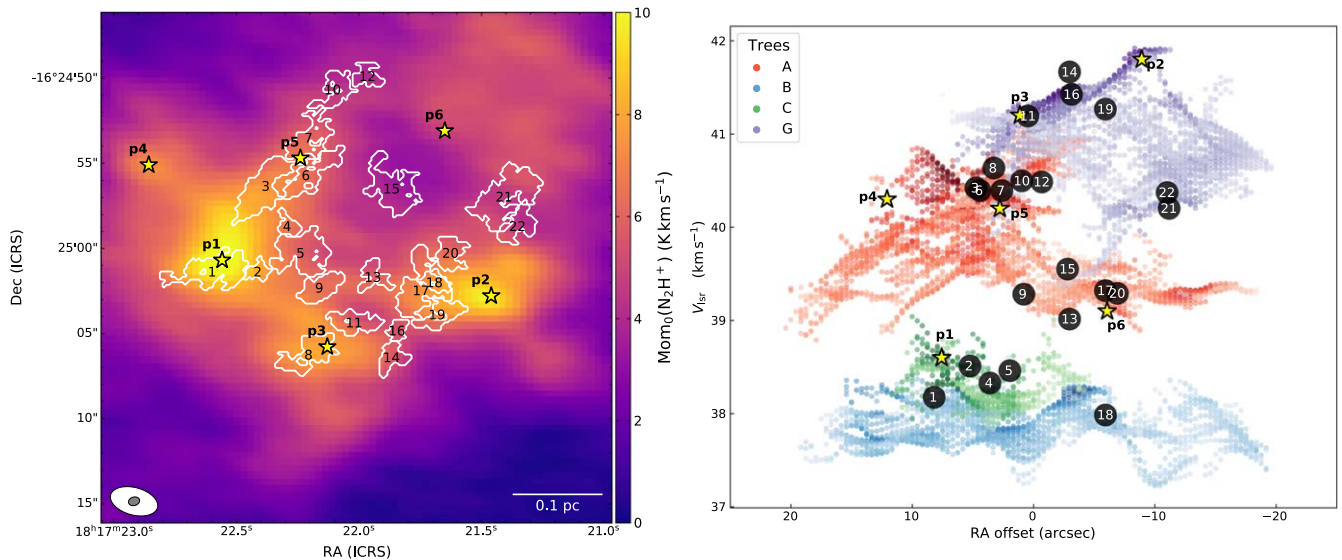


Figure 7. Left panel: The color scale shows the integrated intensity of the isolated N_2H^+ hyperfine component $F_1 = 0-1$. The white contours show the cores identified in $\text{o-H}_2\text{D}^+$ (labeled with numbers), and the star symbols the positions of the protostars (labeled in bold face). The scale bar is indicated in the bottom-right corner. The white ellipse shows the beam size of the N_2H^+ data, while the smaller gray ellipse represents the $\text{o-H}_2\text{D}^+$ beam size. Right panel: position-velocity plot from the results of ACORNS. The plot is the projection in R.A.-velocity space of the 3D plot shown in Figure 9. Right-ascension values are given as offsets with respect to the center of the FoV (position: R.A. = $18^{\text{h}}17^{\text{m}}22^{\text{s}}.05$, decl. = $-16^{\circ}25'01''.7$). The four main trees identified by ACORNS are shown with distinct colors, and the color scale is determined by the peak intensity of the line, stretching linearly between 0 K and 90% of the maximum T_{peak} in each tree. The positions of the prestellar and the protostellar cores are shown with the black circles and the yellow stars, respectively. Labels correspond to those in the left panel.

in the ppv space of the prestellar and protostellar cores. For the prestellar ones, we use the positions of the peak intensity of the $\text{o-H}_2\text{D}^+$ integrated intensity within each core and the centroid velocity at the same position obtained with MCWEEDS (see Section 3.1.2). The properties of the protostellar cores are derived from Li et al. (2020), who used DCO^+ , N_2D^+ , or C^{18}O data to infer the systemic velocity values.¹⁴ A two-dimensional R.A.-velocity plot of the same data is shown in the right panel of Figure 7.

All the four main trees identified by ACORNS appear to be associated with prestellar cores, and at least three of them host protostellar sources. These findings suggest that all of these structures have been or still are active in star formation. The structure at lower V_{lsr} values (shown in blue in Figure 9; labeled B in Figure D1) is the most coherent in velocity, as it span less than 1.0 km s^{-1} , despite extending over $\approx 0.75 \text{ pc}$ on the plane of the sky. It is also the most quiescent in star formation activity, based on the fact that it is associated with only one prestellar core, and no protostar. On the contrary, the tree colored in green in Figure 9 (cluster C in Figure D1), despite having a physical size of $\approx 0.15 \text{ pc}$, contains four cores identified in $\text{o-H}_2\text{D}^+$ and one protostellar core. The presence of tracers of both protostellar activity and of cold and dense gas suggest that the star formation is still on-going, and that the protostellar object is very young. The position of protostellar core p1 is found in fact very close to the $\text{o-H}_2\text{D}^+$ core 1, which hints to the fact that the protostellar envelope is still cold and dense enough to have a detectable abundance of $\text{o-H}_2\text{D}^+$.

The remaining two trees (labels A and G in Figure D1 are shown, respectively, in red and purple in the right panel of Figure 7 and in Figure 9) show a more complex and overlapping structure in the ppv space, and they represent the most dynamically active part of the IRDC clump. At the same

time they contain the large majority of cores identified in $\text{o-H}_2\text{D}^+$ and three protostellar cores. This is indicative of the fact that this region of the clump is dynamically very active.

The two protostellar cores p4 and p6 are not associated in the ppv space with any of the four main trees identified in N_2H^+ . After checking the whole cluster hierarchy found by ACORNS, however, p4 appears to be embedded in one of the minor trees identified (labeled as “r” in Figure D1). Protostellar core p6, instead, has not correspondence in the forest identified by the algorithm. It still emits in the N_2H^+ (1–0) transition (as can be seen in the integrated intensity map shown in Figure 7) but with low flux, hence not fulfilling the S/N threshold that we require in the fitting algorithm. A possible interpretation of this observational evidence is that p6 has still an envelope, but this has been significantly cleared out by the protostellar activity, suggesting that this could be a more evolved protostar with respect to the others.

The tree labeled G (shown in purple in the right panel of Figure 7 and in Figure 9) is one of the largest identified trees, as alone it contains more than 20% of the total data points and $\approx 33\%$ of the total flux. It also presents a significant shift in velocity, extending from $V_{\text{lsr}} = 39.5$ to 42 km s^{-1} . We now focus on its part connecting the two protostars p2 and p3 (see Figure 7), which presents the brightest peak intensities of the N_2H^+ line. This section looks like a filament, elongating between the two protostellar cores, and containing four cores identified in the $\text{o-H}_2\text{D}^+$ data (*n.* 11, 14, 16, and 19). The velocity is increasing from p3 toward p2.

The left panel of Figure 10 shows the map of the peak intensity of points belonging to tree G. The material surrounding and linking the two protostars emits the brightest lines (with $T_{\text{peak}} > 2.5 \text{ K}$) detected in the source. In the right panel of Figure 10, we show the V_{lsr} map of this tree, with overlaid the contours of the outflows detected in the region by Li et al. (2020). The filamentary structure stretching between the two protostellar cores is found in correspondence with the

¹⁴ A 3D interactive copy of this figure is permanently maintained at: http://theory-star-formation-group.cl/sbovino/AG14_n2hp_light.html.

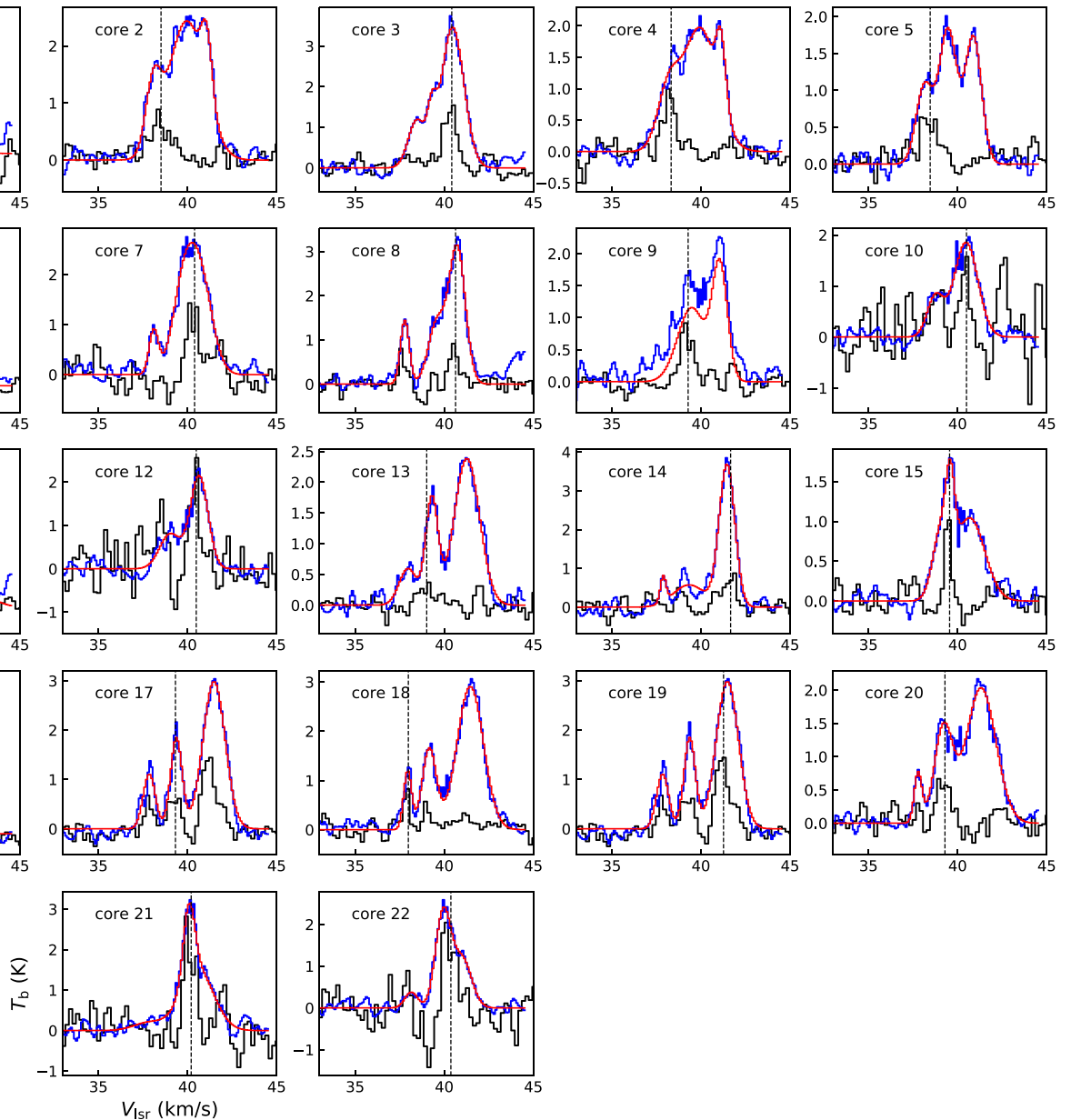


Figure 8. Comparison of the N_2H^+ ($1-0$), in blue, and the $\text{o-H}_2\text{D}^+$ ($1_{1,0}-1_{1,1}$) spectra, in black, at the core positions. The spectra are taken at the position of the peak of $\text{o-H}_2\text{D}^+$ integrated intensity. The red curves show the best model obtained by fitting the N_2H^+ data with three Gaussian components. The centroid velocity of the $\text{o-H}_2\text{D}^+$ is shown with the vertical dashed line in each panel.

red lobe of the outflow powered by protostar p2. However, the two features cannot coincide spatially, as their velocities are opposite: the outflow is redshifted, and it has velocities higher than the local standard of the rest velocity of protostar p2 ($V_{\text{lsr}} = 41.8 \text{ km s}^{-1}$; according to Li et al. 2020), while the gas traced by the N_2H^+ line is found at lower (blueshifted) velocities than that of the protostar. Furthermore, the four H_2D^+ cores embedded in the gas present low velocity dispersion ($\sigma_v = 0.27\text{--}0.34 \text{ km s}^{-1}$) and transonic turbulent Mach number ($\mathcal{M} = 1.2\text{--}1.6$; see Table 2), suggesting that the dense gas embedded in the filamentary structure is still cold and quiescent, and unperturbed by outflows.

We can thus speculate on the possible scenarios that would give raise to such an observed configuration. A first possibility is simply that we are seeing a bulk motion of the gas. The filament-like structure is moving, and the cores embedded into it participate

to this motion. A second possibility is that the gas is flowing toward protostellar core p2 (i.e., toward increasing velocities), and it accretes material onto the protostar, which in turn powers the bipolar outflow. In any case, the red outflow lobe of p2 and the filament-like structure are found on two distinct planes, which intersect at the position of the protostar, and they appear to be overlapping in the R.A.–decl. space only due to projection effects.

Regardless of the real configuration, the observations unveil a gas flow along the filamentary structure, and it is possible to evaluate the mass-flow rate associated to it. If the correct scenario is the second we proposed, we can interpret this quantity as a mass accretion rate onto protostar p2. To perform the calculation, we consider the filament as limited to those positions where $T_{\text{peak}} > 2.5 \text{ K}$, as we want to focus on the denser portion of the gas traced by the N_2H^+ ($1-0$) line. This region, shown with the white contour in the left panel of Figure 10, has a width of

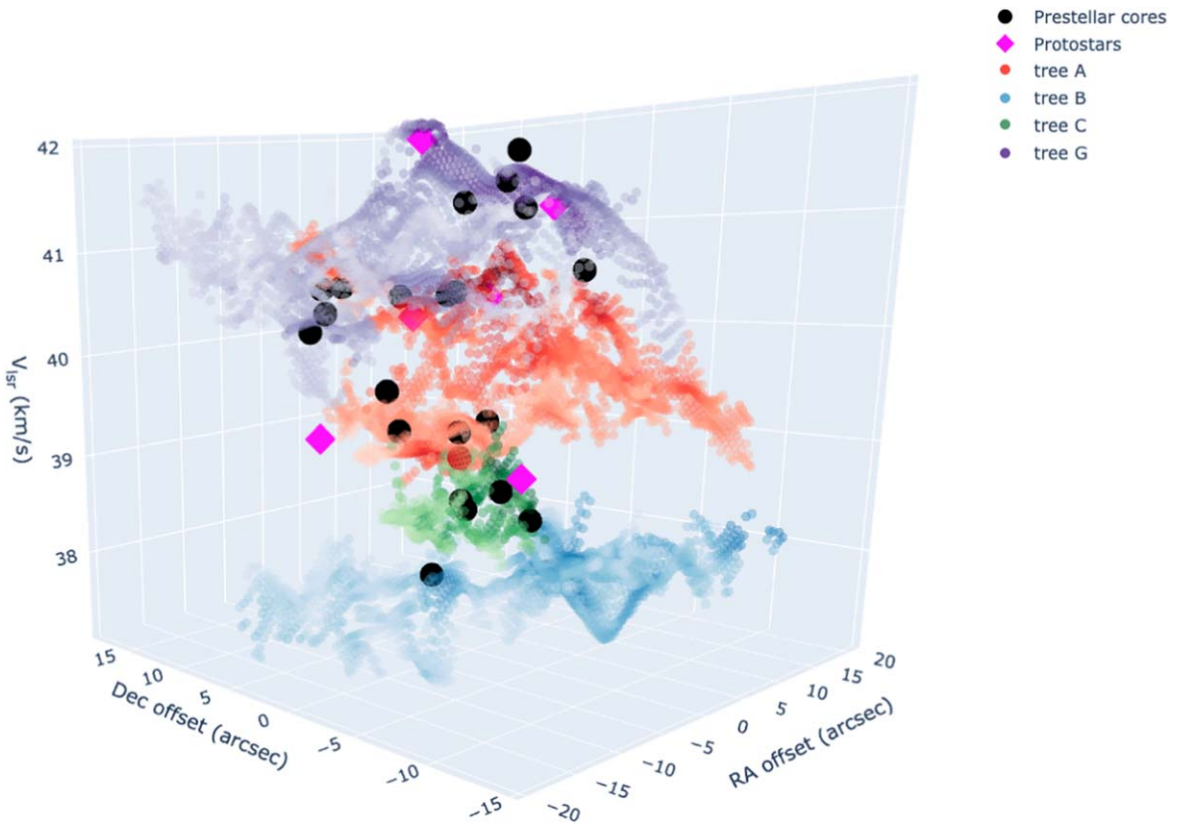


Figure 9. Screenshot of the ppv distribution of the four main trees identified by ACORNS, shown with distinct colors (A: red, B: blue, C: green, G: purple). The color scale within each tree is determined by the peak intensity of the N_2H^+ component. The black dots show the ppv position of the H_2D^+ cores (taken at the peak of the line integrated intensity), while the magenta diamonds represent the positions of the protostellar cores, following Li et al. (2020). A permanent copy of this interactive plot is available at: http://theory-starformation-group.cl/sbovino/AG14_n2hp_light.html. The interactive version allows the reader to rotate the figure, to zoom in and out, and to see the numeric labels of the protostellar and prestellar cores by moving the cursor over.

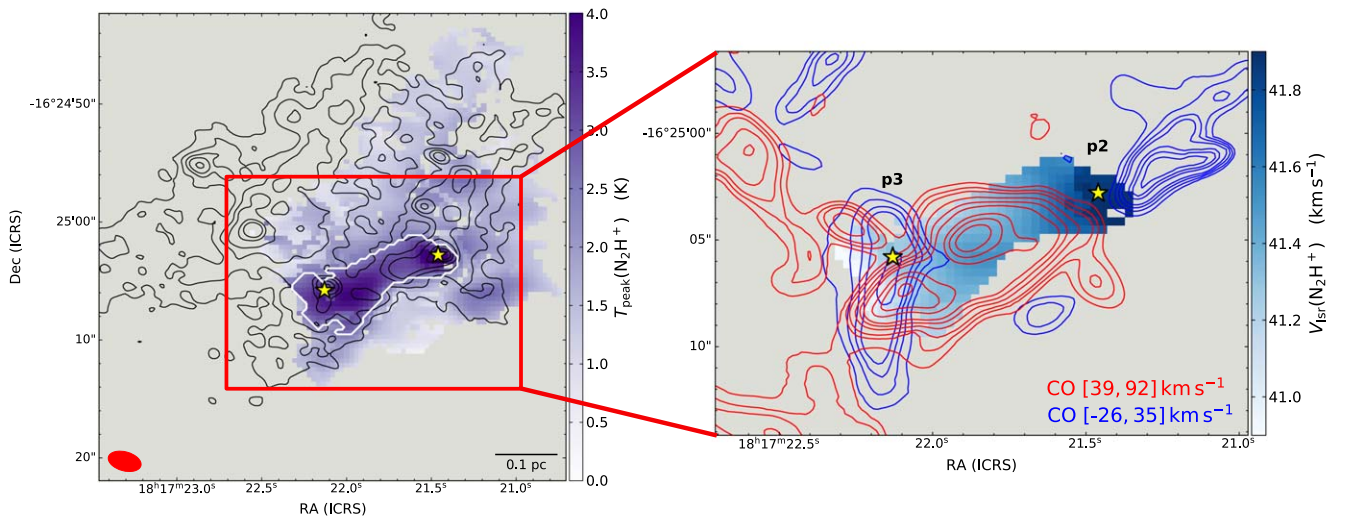


Figure 10. Left panel: The color scale shows the peak intensity of the N_2H^+ components associated with tree G, and the white contour shows the mask (corresponding to $T_{\text{peak}} > 2.5$ K) used to identify the filament studied in Section 3.2. The black contours show the continuum emission at 1.34 mm, at levels [0.5, 1.0, 1.7, 2.5, 4.2, 5.9] mJy beam $^{-1}$ (from Sanhueza et al. 2019). The red box indicates the position of the zoomed area shown in the right panel. Right panel: V_{lsr} map of tree G within the white contour of the left panel, with CO emission overlaid in contours (from Li et al. 2020). The contours are computed in the velocity indicated in the bottom-right corner, at levels: for the blue component, [1.08, 1.62, 2.16, 2.7, 3.78, 4.32, 4.86] Jy beam $^{-1}$ km s $^{-1}$; for the red component, [1.33, 1.995, 2.66, 3.99, 5.32, 6.65, 9.31, 10.64, 11.97] Jy beam $^{-1}$ km s $^{-1}$. The positions of protostars p2 and p3 are shown with yellow stars in both panels.

0.08–0.12 pc, which are typical values for filaments (see, e.g., Arzoumanian et al. 2011, 2019; Palmeirim et al. 2013; Sabatini et al. 2019), and a length of ≈ 0.26 pc. It spans 1 km s $^{-1}$ in velocity, from 40.9 km s $^{-1}$ close to protostar p3 to 41.9 km s $^{-1}$ around p2. The velocity gradient is hence $\nabla V = 3.85$ km s $^{-1}$ pc $^{-1}$.

To estimate the total mass of the filament (M_{fil}), we again employ Equation (5). We use the continuum emission detected in Band 6 at 1.34 mm, as its FoV and resolution are closer to those of the Band 3 data with respect to the Band 7 ones. The flux density contained within the mask shown in Figure 10 is $F_{\text{fil}} = 85$ mJy. A

significant contribution to this flux level comes from the bright emission of cores p2 and p3, which are 16 and 15 mJy, respectively (Sanhueza et al. 2019). In these cores, the emission likely arises from the warmer envelope surrounding the protostellar object, and we hence subtract it from F_{fil} , as we are interested in the flow of gas not associated with the envelope of the protostars. The dust opacity at 1.34 mm, computed following Equation (6), is $0.81 \text{ cm}^2 \text{ g}^{-1}$. Assuming $T_{\text{dust}} = 10 \text{ K}$, we obtain $M_{\text{fil}} = 57 M_{\odot}$. The mass accretion rate is then $\dot{M}_{\text{acc}} = M_{\text{fil}} \times \nabla V = 2.2 \times 10^{-4} M_{\odot} \text{ yr}^{-1}$. We stress again that this is the rate at which the mass flows along the filamentary structure. The scenario in which it actually corresponds to an accretion motion is only one of the possibilities that would explain the observations. In order to definitely assess if this is the case, more information, in particular on the protostars (i.e., their masses, luminosities, evolutionary stages, etc.) would be helpful.

In the following, we discuss the sources of uncertainties that affect the physical quantities just determined. First of all, there is the uncertainty on the mass, which accounts for $\approx 40\%$ (see Section 3.1.4), that comes from uncertainties in the dust-to-gas ratio, in the source's distance, and in the dust opacity. Furthermore, the inclination i of the filament with respect to the plane of the sky is unknown, and it affects the value of \dot{M}_{acc} by a factor $\tan i$ (see, e.g., Chen et al. 2019). If the inclination varies in the range 30° – 60° , the derived value of the accretion rate changes up to 70%. Due to these considerations, with a conservative approach we assume that the derived \dot{M}_{acc} value is correct within a factor of 2. Within the uncertainties, the value we found is in agreement with measurements in similar sources: for instance, Lu et al. (2018) found $\dot{M}_{\text{acc}} = (1\text{--}2) \times 10^{-4} M_{\odot} \text{ yr}^{-1}$ in filaments belonging to four high-mass star-forming regions, while Chen et al. (2019) derived $\dot{M}_{\text{acc}} = (0.2\text{--}1.3) \times 10^{-4} M_{\odot} \text{ yr}^{-1}$ in several filaments identified in the infrared dark cloud G14.225-0.506. Sanhueza et al. (2021) derived $\dot{M}_{\text{acc}} = (0.9\text{--}2.5) \times 10^{-4} M_{\odot} \text{ yr}^{-1}$ in a hot core embedded in the high-mass star-forming region IRAS 18089-1732, even though at smaller spatial scales ($\approx 10,000 \text{ au}$). In Li et al. (2022), authors studied the accretion in a filament in the high-mass star-forming region NGC6334S, deriving $\dot{M}_{\text{acc}} = 0.3 \times 10^{-4} M_{\odot} \text{ yr}^{-1}$. Furthermore, this value is also in agreement with the results of numerical simulations (see, e.g., Wang et al. 2010; Kuiper et al. 2016).

The critical line mass of a filament, in the approximation of isothermal cylindrical shape, is (Ostriker 1964):

$$m_c = \frac{2c_s^2}{G} = 17 \left(\frac{T_K}{10 \text{ K}} \right) M_{\odot} \text{ pc}^{-1}. \quad (8)$$

The line mass of the filamentary-like structure in AG14 is $m = M_{\text{fil}}/L_{\text{fil}} = 220 M_{\odot} \text{ pc}^{-1}$, i.e., significantly higher than its critical value, which suggests that this structure is not in hydrostatic equilibrium. One could naturally wonder whether this is consistent with the possible scenario of accretion flow that has been discussed. In particular, it is worth comparing the timescales for accretion (t_{acc}) and free-fall collapse (t_{ff}), at least in terms of orders of magnitude. The former can be approximated by the ratio between the mass reservoir and the accretion rate: $t_{\text{acc}} = M_{\text{fil}}/\dot{M}_{\text{acc}} = 2.6 \times 10^5 \text{ yr}$. To estimate the time necessary for a filament to fully collapse onto its axis, we use Equation (18) of Hacar et al. (2022), which in turn was

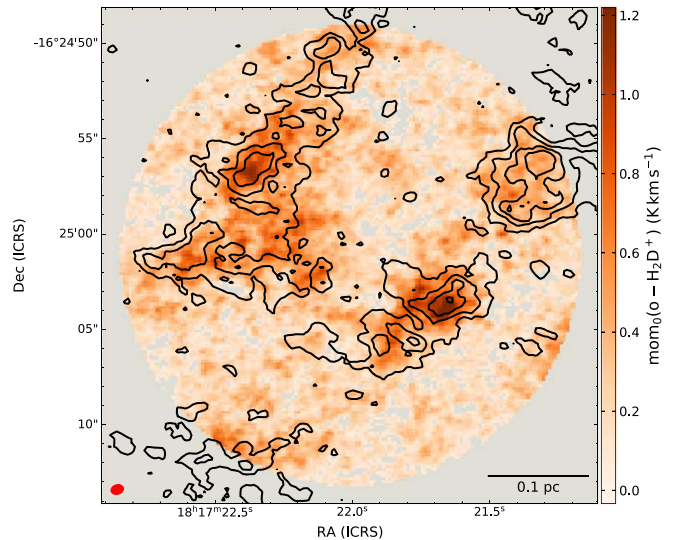


Figure 11. The color scale shows the integrated intensity of the $\text{o-H}_2\text{D}^+(1_{1,0}\text{--}1_{1,1})$ transition as in Figure 1. The black contours show the $\text{N}_2\text{D}^+(3\text{--}2)$ integrated intensity (computed as for $\text{o-H}_2\text{D}^+$; see Section 2). The levels are: $[7, 11, 15, 19]\sigma$, where $1\sigma = 100 \text{ mK km s}^{-1}$.

derived from Pon et al. (2012) and Toalá et al. (2012):

$$t_{\text{ff}} = 1.9 \left(\frac{L_{\text{fil}}}{\text{FWHM}_{\text{fil}}} \right)^{0.5} \left(\frac{n_0}{10^3 \text{ cm}^{-3}} \right)^{-0.5} \text{ Myr}, \quad (9)$$

where $L_{\text{fil}}/\text{FWHM}_{\text{fil}} = 2.6$ is the filament aspect ratio (i.e., the ratio between its length $L_{\text{fil}} = 0.26 \text{ pc}$ and its width $\text{FWHM}_{\text{fil}} = 0.1 \text{ pc}$), and n_0 is the filament central density at the spine. As we are interested only in a rough estimation of this quantity, we test the range of densities found in the cores¹⁵, i.e., $n_0 = 10^5\text{--}10^6 \text{ cm}^{-3}$, obtaining $t_{\text{ff}} = 1\text{--}3 \times 10^5 \text{ yr}$. We conclude that the two timescales are comparable, and hence the filament would have time to accrete a significant fraction of its mass onto p2 before collapsing.

3.3. Comparison between $\text{o-H}_2\text{D}^+$ and N_2D^+

The cores identified in Section 3.1.1 using $\text{o-H}_2\text{D}^+$ data are formed by cold and dense gas that should be in a prestellar stage, even though we have evidence that a minority of cores are found in close proximity to protostellar cores (in the ppv space), such as core 1 (close to protostar p1), or cores 3, 6, and 7 (close to p5). We can speculate that in these cases the $\text{o-H}_2\text{D}^+$ emission is tracing the part of the protostellar envelopes that is still cold enough that the desorption of CO from the dust grains has not happened yet. This is confirmed by depletion maps derived from $\text{C}^{18}\text{O}(2\text{--}1)$ observations of AG14 at $1''/3$ of resolution, which show that the depletion factor is high ($f_D > 50$) even around protostellar cores (Sabatini et al., 2022). This suggests that ALMA observations at resolution of $\approx 1''$ are tracing the dense and still cold envelope around protostellar objects, where the feedback of the protostar has not affected the gas yet. However, even the remaining cores could still belong to distinct evolutionary stages. To these regards, we have mentioned that Giannetti et al. (2019) studied the

¹⁵ This values are also consistent with the average density of the filament, computed assuming that it is a perfect cylinder of length L_{fil} and radius FWHM_{fil} .

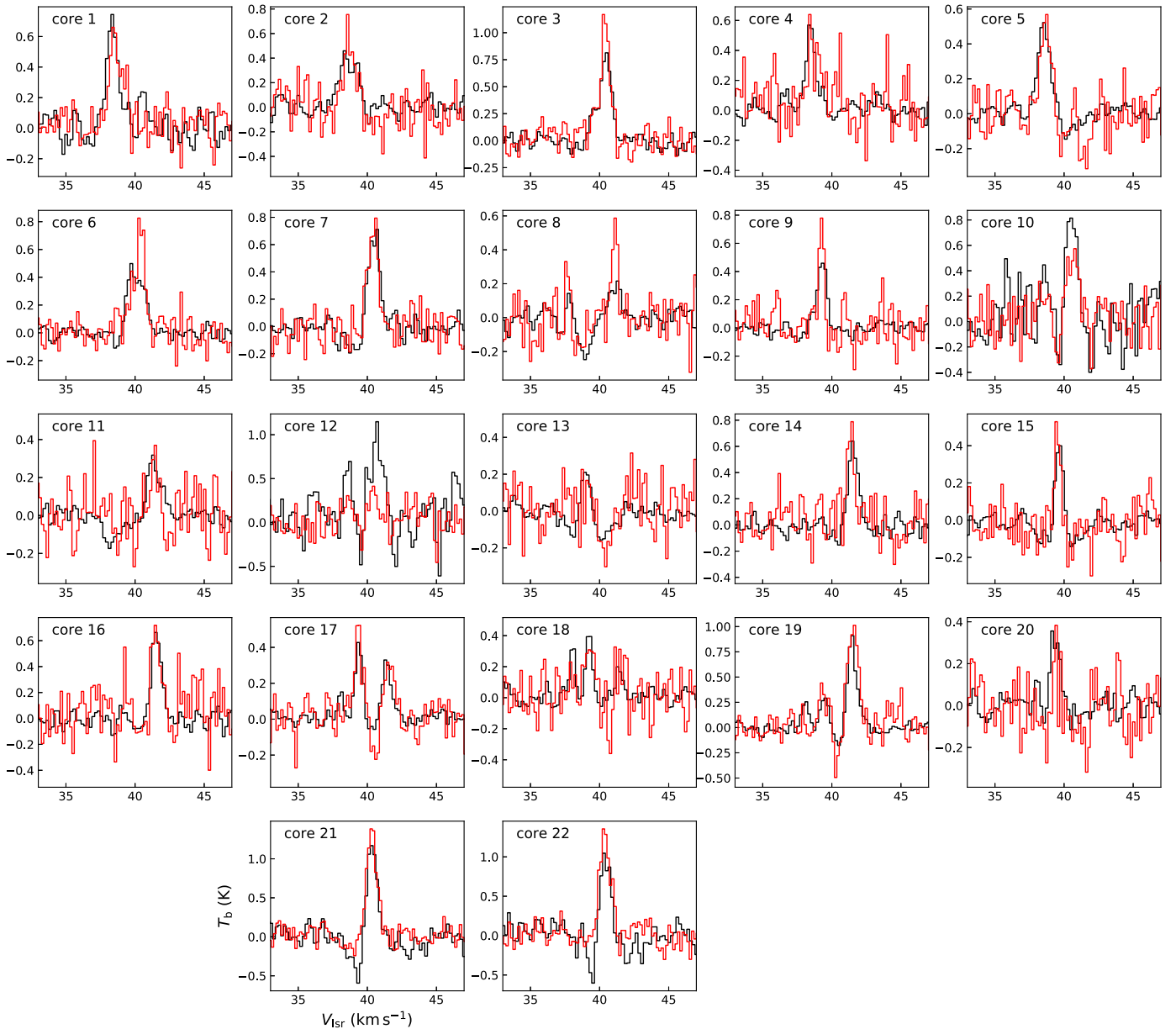


Figure 12. Comparison between the average N_2D^+ (3–2) and $\text{o-H}_2\text{D}^+$ ($1_{1,0}$ – $1_{1,1}$) lines in each core (labeled at the top-left corner of each panel). The N_2D^+ data are shown with the red histograms, while the $\text{o-H}_2\text{D}^+$ ones are shown with the black curves. Note that the $\text{o-H}_2\text{D}^+$ data have been smoothed to the same beam size of the N_2D^+ cube before extracting the average spectra, which thus are not identical to the ones presented in Figure 5.

correlation between the $\text{o-H}_2\text{D}^+$ ($1_{1,0}$ – $1_{1,1}$) and the N_2D^+ (3–2) transitions in three clumps embedded in the G351.77–0.51 complex, using single-dish data from APEX. The main result of those authors was an anticorrelation between the abundances of the two molecular species, possibly due to evolutionary effects. Their findings hinted to the possibility of using the abundance ratio between N_2D^+ and $\text{o-H}_2\text{D}^+$ as an evolutionary indicator.

In Figure 11 we show the comparison between the integrated intensities of the N_2D^+ (3–2) and the $\text{o-H}_2\text{D}^+$ ($1_{1,0}$ – $1_{1,1}$) transitions. The two tracers appear to be quite correlated spatially, but some differences are visible. For instance, in the northwest part of the source, the N_2D^+ line has a bright peak, which is not seen in $\text{o-H}_2\text{D}^+$. Furthermore, the N_2D^+ transition seems more extended, even though we must highlight a possible observational bias: despite we excluded the Total

Power observations from the Band 6 data set, its maximum recoverable scale is still almost twice that of the $\text{o-H}_2\text{D}^+$ data, hence making the former more sensitive to large-scale emission.

In order to further explore the comparison at the core level, we compared the average spectra of $\text{o-H}_2\text{D}^+$ ($1_{1,0}$ – $1_{1,1}$) and N_2D^+ (3–2) in each core. As the Band 6 data have a lower resolution of $1''.4 \times 1''.0$, we first smoothed the Band 7 data to this beam size, to allow for a proper comparison. Both spectral cubes have been regridded to the same coordinate grid. The spectral resolution of the two data sets is comparable (0.20 km s^{-1} for $\text{o-H}_2\text{D}^+$ and 0.17 km s^{-1} for N_2D^+). The comparison of the average spectra is shown in Figure 12. The similarities between the line profiles of the two tracers are remarkable, both in terms of intensity and of line shapes. In four cores (12, 13, 18, and 20), the N_2D^+ transition is not detected above the 3σ level, but we highlight that the rms of

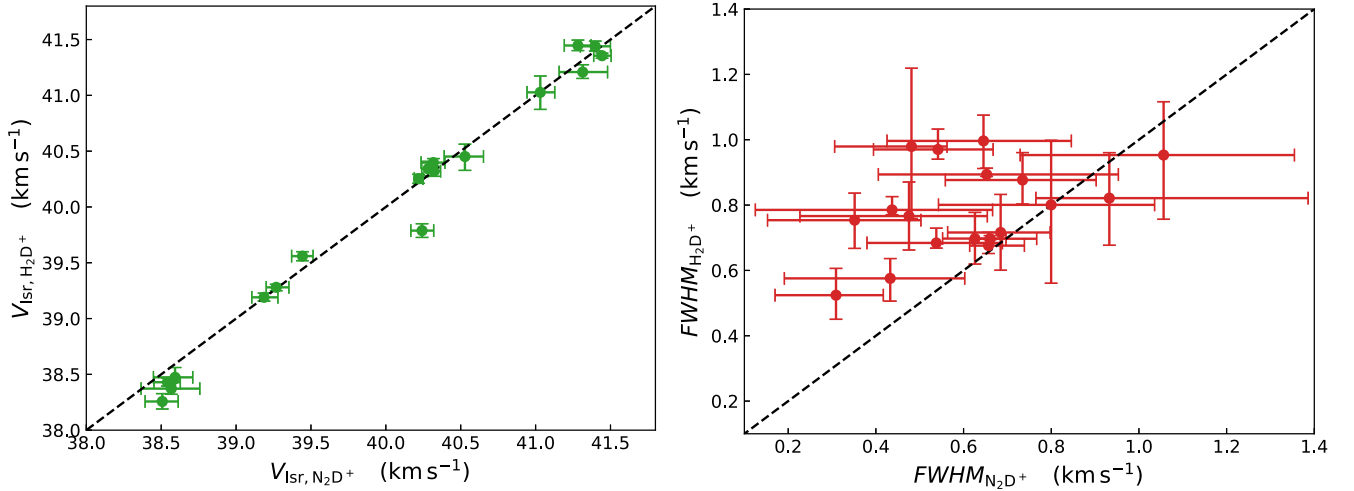


Figure 13. Left panel: comparison of the centroid velocities obtained with MCWEEDS on the N_2D^+ and $\text{o-H}_2\text{D}^+$ average spectra in the cores where both species have been detected above the 3σ level. The black dashed line shows the 1:1 relation. Right panel: same as in the left panel but for the line widths.

the N_2D^+ spectra is on average ≈ 2.5 times worse than in the corresponding $\text{o-H}_2\text{D}^+$ spectra.

We have fitted the average spectra shown in Figure 12 with MCWEEDS. We assumed $T_{\text{ex}} = 10$ K also for N_2D^+ , for which we take the hyperfine splitting due to the ^{14}N nuclei into consideration, according to the CDMS database. Figure 13 shows the comparison of the best-fit values for the centroid velocity and FWHM for the two tracers in the cores where both are detected above 3σ . The V_{lsr} values align very well, considering the uncertainties, with the 1:1 relation (shown with the black dashed curve), highlighting that the two molecular emissions arise from similar spatial regions within the source. Concerning the line widths, the right panel of Figure 13 shows that for 80% of the cores the $\text{o-H}_2\text{D}^+$ transition presents broader lines with respect to N_2D^+ . This can be partially due to opacity effect, as the $\text{o-H}_2\text{D}^+(1_{1,0}-1_{1,1})$ can be moderately optically thick, leading to a 15% overestimation of the line width (see Appendix C). The presence of the hyperfine splitting in the N_2D^+ ($3-2$) transition, instead, reduces this problem. Furthermore, we highlight the difference in the critical density of these two tracers (1 order of magnitude higher for the N_2D^+ line than for the $\text{o-H}_2\text{D}^+$ transition).

In Figure 14 we report the correlation between the column density values of $\text{o-H}_2\text{D}^+$ and N_2D^+ . For the cores undetected in N_2D^+ , we report the 3σ upper limits computed based on the rms in each core and the average line widths of the detected cores ($\langle \text{FWHM} \rangle = 0.62 \text{ km s}^{-1}$). We found a discrepancy with the anticorrelation trend found by Giannetti et al. (2019), as the column densities of N_2D^+ and $\text{o-H}_2\text{D}^+$ appear to be well correlated, for the cores detected in both tracers. However, we highlight a fundamental difference between our analysis and that of Giannetti et al. (2019). Those authors selected cores in continuum emission and then analyzed the molecular emission. Our analysis, instead, is intrinsically biased toward cores with bright $\text{o-H}_2\text{D}^+$ emission, as we used this species to identify core-like substructures. Furthermore, Giannetti et al. (2019) investigated the clump level scales, and therefore the anticorrelation reflected averaged clump properties. In this work, on the contrary, we resolve the core scales in a highly dynamically active environment, which further complicate a direct comparison between the two works.

It is worth commenting on the four cores undetected in N_2D^+ emission. They present narrow $\text{o-H}_2\text{D}^+$ lines

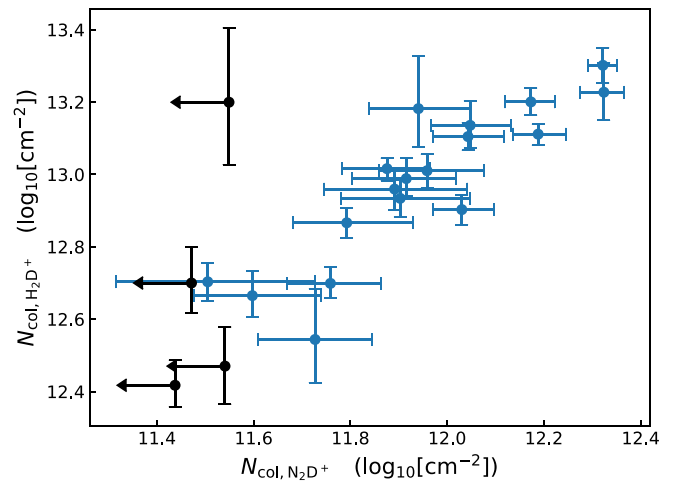


Figure 14. Same as Figure 13 but for the column densities. For the four cores where N_2D^+ is not detected, we show upper limits (in black).

($\sigma_v = 0.18-0.27 \text{ km s}^{-1}$, smaller than the average velocity dispersion of all cores in the clump), hinting to cold and quiescent gas. According to the analysis of the continuum emission (see Section 3.1.4 and Table 3), three of them are undetected in continuum emission, and the last one (18) is the least massive of the sample ($M_{\text{core}} \lesssim 1.0 M_{\odot}$). The nondetection of N_2D^+ can be then explained by two scenarios: (i) these cores are not dense enough to excite the N_2D^+ transition that has an higher critical density with respect to that of the $\text{o-H}_2\text{D}^+(1_{1,0}-1_{1,1})$ line; (ii) alternatively, the lack of continuum emission can be explained if the gas and dust temperatures are so low (< 10 K) that the dust thermal emission at 0.8 mm is not bright; in this case, the cores would be in early evolutionary stage, and perhaps the N_2D^+ , a late-type species, has not yet formed in detectable quantities. In this case, the core masses estimated in Section 3.1.4 could be underestimated.

4. Discussion and Conclusions

In this work, we have investigated the dynamical and kinematic properties of AG14, from the core to the clump scales, analyzing ALMA data at spatial resolutions from

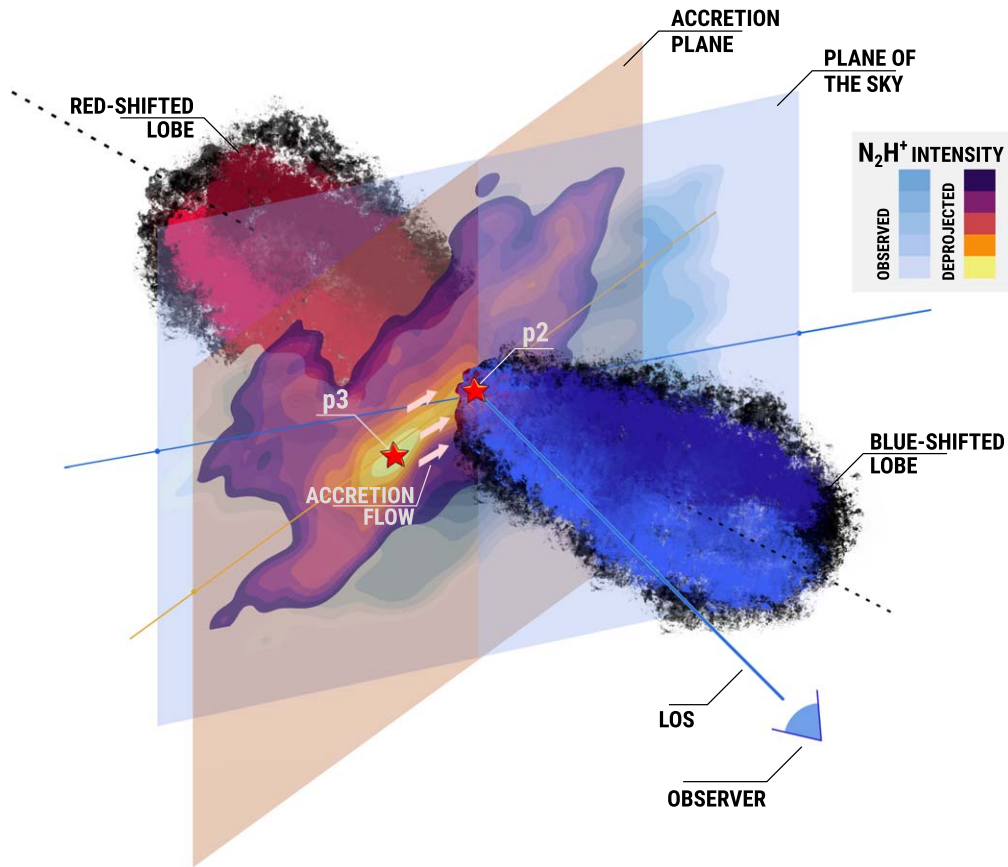


Figure 15. A graphic illustration of the possible 3D configuration that gives rise to the observed structure in Figure 10. A filamentary structure seen in N_2H^+ (1–0) emission accretes material toward protostellar core p2. This launches a bipolar outflow likely almost perpendicularly to the accretion flow. The red lobe, when projected on the plane of the sky, appears to coincide with the filament.

~ 2000 to $\sim 12,000$ au (0.01–0.06 pc). Using Band 7 $o\text{-H}_2D^+$ data, we have identified 22 cores with dendrogram analysis. Comparing their distribution with the dust thermal emission in the same band, most bright continuum peaks are found outside or right at the edge of the H_2D^+ cores. Several of these peaks are known to be associated with outflow activity and therefore are likely protostars. The fact that they lack $o\text{-H}_2D^+$ emission can be explained if they are already quite evolved, and the protostellar feedback has heated the surrounding gas above the CO desorption temperature. If CO is back into the gas phase, its fast reaction with H_2D^+ would lower the abundance of the latter below the detection level. Alternatively, if they are in earlier evolutionary stage and they are still dense and cold, H_2D^+ could be efficiently transformed into its doubly and triply deuterated forms, or it could be depleted due to the depletion of HD itself (Sipilä et al. 2013).

The identified cores have typical masses of $M_{\text{core}} \lesssim 30 M_{\odot}$, and they appear to be subvirial at $T = 10$ K, even though the virial parameters might be underestimated (see Section 3.1.4 for more details). Our data seem to exclude the existence of HMPCs in AG14, even though our mass values could be underestimated due either to the filter-out of large-scale emission by the interferometer, or due to overestimation of the dust temperature. However, the $o\text{-H}_2D^+$ line adds no support for temperatures lower than 10 K, unlike in AG351 and AG354, where a significant fraction of pixels presented lines narrower than the thermal broadening at 10 K (see Redaelli et al. 2021).

The $o\text{-H}_2D^+(1_{1,0}\text{--}1_{1,1})$ transition at the clump level spans a range of $\approx 4 \text{ km s}^{-1}$ in V_{LSR} , and its morphology suggests that multiple velocity components are present in the source. In order to study the large-scale clump kinematics of the gas in which the identified cores are embedded, we used ALMA Band 3 observations of the N_2H^+ (1–0), which is an ideal probe for the large-scale kinematics. From the spectral comparison of the two tracers (the first ever done in the literature, to our knowledge), we can link kinematically each H_2D^+ core with one velocity component of the N_2H^+ spectra. The high-density cores are hence formed in the large-scale gas traced by N_2H^+ , and they inherit its kinematics. The N_2H^+ lines are on average broader than the corresponding $o\text{-H}_2D^+(1_{1,0}\text{--}1_{1,1})$ components, suggesting that the denser gas is more quiescent, as expected from turbulence dissipation.

To disentangle the complex kinematics shown by the N_2H^+ data and to identify its hierarchical structure in the ppv space, we have first fitted the isolated hyperfine component $F_1 = 1\text{--}0$ using a three-component Gaussian fit, and then we have used the results as input for the ACORNS package (Henshaw et al. 2019). The four main trees found by ACORNS are associated with cores identified in $o\text{-H}_2D^+$ emission, and at least three also host protostellar cores, suggesting that all of them are active in star formation. One of the trees (labeled B) presents a small velocity gradient ($\approx 1 \text{ km s}^{-1}$ over 0.75 pc), and it appears to be more quiescent than the others, as it contains only one prestellar core. Interestingly, this core (18) is one of those not detected in N_2D^+ , which can be explained if it is at an early

evolutionary stage, when N_2D^+ —a late-type molecule—did not have the time yet to form. This tree can then represent a less evolved component with respect to the others in the clump.

The trees labeled A and G are associated with more than 70% of the $\text{o-H}_2\text{D}^+$ cores and three protostellar cores, and they are overlapping and intertwined in the ppv space. Such a morphology could be indicative of a sort of competitive accretion scenario, where in the crowded environment of this high-mass clump, multiple low-mass cores ($M_{\text{core}} < 30 M_{\odot}$) have formed. The intraclump gas in which the cores are embedded could provide the cores with the mass reservoir needed to later form high-mass stars. This is also consistent with the fact that at 10 K all the cores are subvirial.

The brightest part of tree G, is structured as a filamentary structure connecting the two protostellar cores p3 and p2. The N_2H^+ centroid velocity increases from $\sim 41 \text{ km s}^{-1}$ close to p3 to $\sim 42 \text{ km s}^{-1}$ close to p2. On the plane of the sky, this structure overlaps with the red lobe of the CO outflow identified by Li et al. (2020). However, the outflow velocities are opposite to that of the N_2H^+ filament, as they are redshifted with respect to the systemic velocity of p2 (42.8 km s^{-1}). We have speculated on the possibilities that would explain the observed configuration, and we show one of them in Figure 15. The filamentary structure seen in N_2H^+ emission might be accreting mass onto protostellar core p2, which then powers a bipolar outflow in a direction likely perpendicular to that of the accretion flow; the red lobe of the bipolar outflow, when seen projected on the plane of the sky, appears to be overlap the N_2H^+ feature, but the two are actually separated in the 3D space. Assuming this scenario, we have computed the mass accretion rate along the filamentary structure, obtaining $\dot{M}_{\text{acc}} = 2.2 \times 10^{-4} M_{\odot} \text{ yr}^{-1}$, expected to be accurate within a factor of 2, in good agreement with other observations in similar sources. From the outflow parameters, Li et al. (2020) estimated a mass accretion rate on protostar p2 of $3\text{--}4 \times 10^{-6} M_{\odot} \text{ yr}^{-1}$, i.e., approximately 2 orders of magnitude lower than our estimate, but this value depends on several assumption (e.g., on the wind velocity and on the ratio between the mass accretion rate and the mass ejection rate). Furthermore, the value of Li et al. (2020) represents the accretion rate onto the protostar, while we compute the rate onto the core.

In this work, we have shown how ALMA observations of several molecular tracers are a powerful diagnostic tool to investigate the fragmentation and kinematic properties of the high-mass clump AG14. In particular, $\text{o-H}_2\text{D}^+$ appears to be an ideal tracer of the cold and dense gas, and as such it can be used to identify cores likely in an early evolutionary stage. On the other hand, Band 3 data of N_2H^+ can be used to trace the gas kinematics at clump scales and at the clump-to-core transition, providing important information on the dynamics and accretion properties of the gas from which the cores formed.

The authors thank the anonymous referee for the comments which helped to improve the quality of the manuscript. The authors acknowledge Tommaso Grassi for the help in producing Figure 15. ER acknowledges the support from the Minerva Fast Track Program of the Max Planck Society. E.R. and P.C. acknowledge the support of the Max Planck Society. S.B. is financially supported by ANID Fondecyt Regular (project #1220033), and the ANID BASAL projects ACE210002 and FB210003. P.S. was partially supported by a Grant-in-Aid for Scientific Research (KAKENHI No. 18H01259 and 22H01271).

This paper makes use of the following ALMA data: ADS/JAO.ALMA#2018.1.00331.S, ADS/JAO.ALMA#2015.1.01539.S, ADS/JAO.ALMA#2018.1.00299.S. ALMA is a partnership of ESO (representing its member states), NSF (USA) and NINS (Japan), together with NRC (Canada), MOST and ASIAA (Taiwan), and KASI (Republic of Korea), in cooperation with the Republic of Chile. The Joint ALMA Observatory is operated by ESO, AUI/NRAO and NAOJ. This research made use of ASTRODENDRO, a Python package to compute dendrograms of Astronomical data (<http://www.dendrograms.org/>).

Software: SCIMES (Colombo et al. 2015), MCWEEDS (Giannetti et al. 2017), PyMC (Patil et al. 2010), PYSPECKIT (Ginsburg & Mirocha 2011), ACORNS (Henshaw et al. 2019), ASTRODENDRO (<http://www.dendrograms.org/>).

Appendix A

Core Identification in Continuum Emission

In Section 3.1.1 it has been discussed how the morphology of the continuum emission and of the $\text{o-H}_2\text{D}^+$ integrated intensity do not correlate. To strengthen this point, we have performed a core identification also in the dust thermal emission, similarly to what was done in Appendix B of Redaelli et al. (2021). We highlight that Sanhueza et al. (2019) already performed a core-finding analysis in the clump, using the continuum data in Band 6, which have a sensitivity ≈ 4 times higher than the Band 7 data. We however prefer to use the continuum at 0.8 mm to perform the comparison with the $\text{o-H}_2\text{D}^+$ analysis, as these two data sets were observed with the same ALMA configuration.

As SCIMES works in the ppv space, we used the PYTHON package ASTRODENDRO, on which SCIMES is based, to analyze the 2D continuum map. Concerning the input parameters necessary to perform the clustering, we set $\Delta_{\text{min}} = 1 \times \text{rms}$ ($\text{rms} = 0.5 \text{ mJy pix}^{-1}$ for the nonprimary-beam-corrected map); the minimum value to identify structures is $\text{min}_{\text{val}} = 2.5 \times \text{rms}$; the identified cores must be larger than 3 times the beam size, in order to be consistent with the identification of the $\text{o-H}_2\text{D}^+$ cores.

With these inputs, ASTRODENDRO identifies 11 cores, shown in Figure A1. Four of them (c1, c3, c6, and c11) are found in correspondence with the protostellar candidates. Five cores (22%) seen in $\text{o-H}_2\text{D}^+$ do not correspond to continuum-identified structures, which suggests that they are in a very early stage, and their low temperatures translates in low continuum fluxes at 0.8 mm. In turn, continuum core c8 does not overlap with any structure seen in $\text{o-H}_2\text{D}^+(1_{1,0}\text{--}1_{1,1})$. This structure corresponds to core 5 in the analysis of Sanhueza et al. (2019) and Li et al. (2020). The latter paper does not consider it as associated with clear outflow emission, even though it shows evidence of CO emission at high velocities. Furthermore, Sanhueza et al. (2019) lists it among the cores with emission from high-energy transitions. It is hence possible that core c8 hosts a young protostar, that either does not power outflow, or that cannot be detected due, for instance, to projection effects.

Core c3 is the largest one, but it contains three separated flux peaks. It is likely that the algorithm is not able to separate them due to the limited sensitivity of our data. In fact, in Sanhueza et al. (2019) two separated cores were identified in this area in the 1.34 mm continuum emission. In this scenario, core c3 is hence divided in two parts, one which is in a protostellar stage and does not show significant $\text{o-H}_2\text{D}^+$

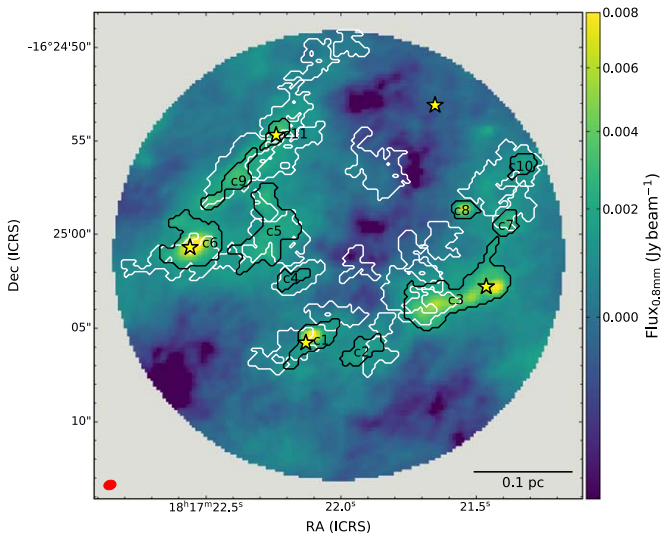


Figure A1. The color scale shows the continuum emission in Band 7. The white contours represent the $\text{o-H}_2\text{D}^+$ cores, while the black ones show the cores identified in continuum, which are labeled based on increasing decl.. The beam size and scale bar are shown in the bottom left and right corners, respectively. Cores associated with outflow emission according to Li et al. (2020) are shown with stars.

emission; the other instead is in an earlier evolutionary stage, and it overlaps with several cores seen in $\text{o-H}_2\text{D}^+$. Core c6 is peculiar, in the sense that it overlaps significantly ($>50\%$) with $\text{o-H}_2\text{D}^+$ core 1, and it also contains a protostar. As already suggested in Section 3.2, these features suggest that this protostar is young, still embedded in a thick envelope that is relatively cold to have a detectable abundance of $\text{o-H}_2\text{D}^+$.

In conclusion, more than half of the $\text{o-H}_2\text{D}^+$ identified cores overlap with continuum cores by less than 30% of their physical extension. This is likely due to different evolutionary stages traced by the two data sets. While the $\text{o-H}_2\text{D}^+$ emission trace cold gas still relatively undisturbed by protostellar activity, the continuum data cannot distinguish between cores in the prestellar and protostellar phases. We note that Sanhueza et al. (2019) already identified cores in the continuum. We prefer to redo this analysis, as the Band 6 data used in that paper have a worse resolution (by a factor of ≈ 2.0) and a larger maximum recoverable scale (by $\approx 50\%$) than our Band 7 data, and we prefer to analyze a data set acquired with the same interferometer configuration as the $\text{o-H}_2\text{D}^+(1_{1,0}-1_{1,1})$ data. We have however checked that the two methods identifying cores in the continuum produce results in reasonable agreement. By comparing the cores found in this appendix and in Sanhueza et al. (2019; figure not shown here), 10 out of the 11 cores we identify have correspondence to structures seen in Band 6. In the FoV where the two data sets overlap, Sanhueza et al. (2019) found more cores, also due to the better sensitivity of their data set. However, several of the H_2D^+ -identified cores (5 out of 22) still have no clear correspondence with continuum-identified structures, and our conclusion that continuum and line morphologies are different still holds.

Appendix B

Results of the Spectral Fit of the $\text{o-H}_2\text{D}^+(1_{1,0}-1_{1,1})$ Transition in Each Core

Figures B1 to B4 present the maps of the best-fit parameters obtained with MCWEEDS in each core. Concerning the line widths, here we show the FWHM maps, which is the actual free parameter used in the fitting procedure.

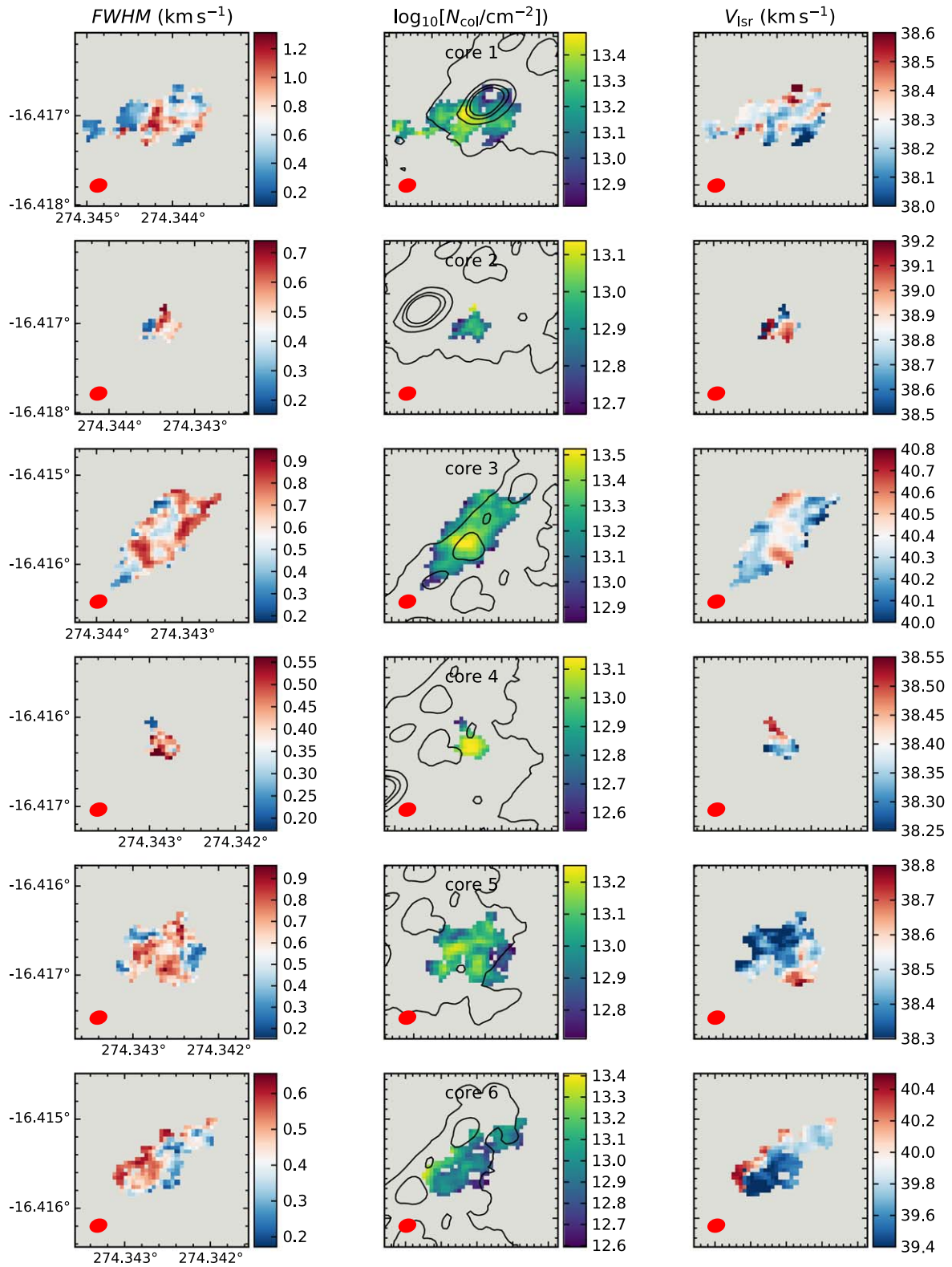


Figure B1. Maps of best-fit parameters obtained with MCWEEDS. The columns are FWHM, N_{col} , and V_{lsr} , from left to right. The core label is indicated at the top of each central panel. The contours show the continuum emission at levels from 2 to 11 σ , in steps of 3 σ .

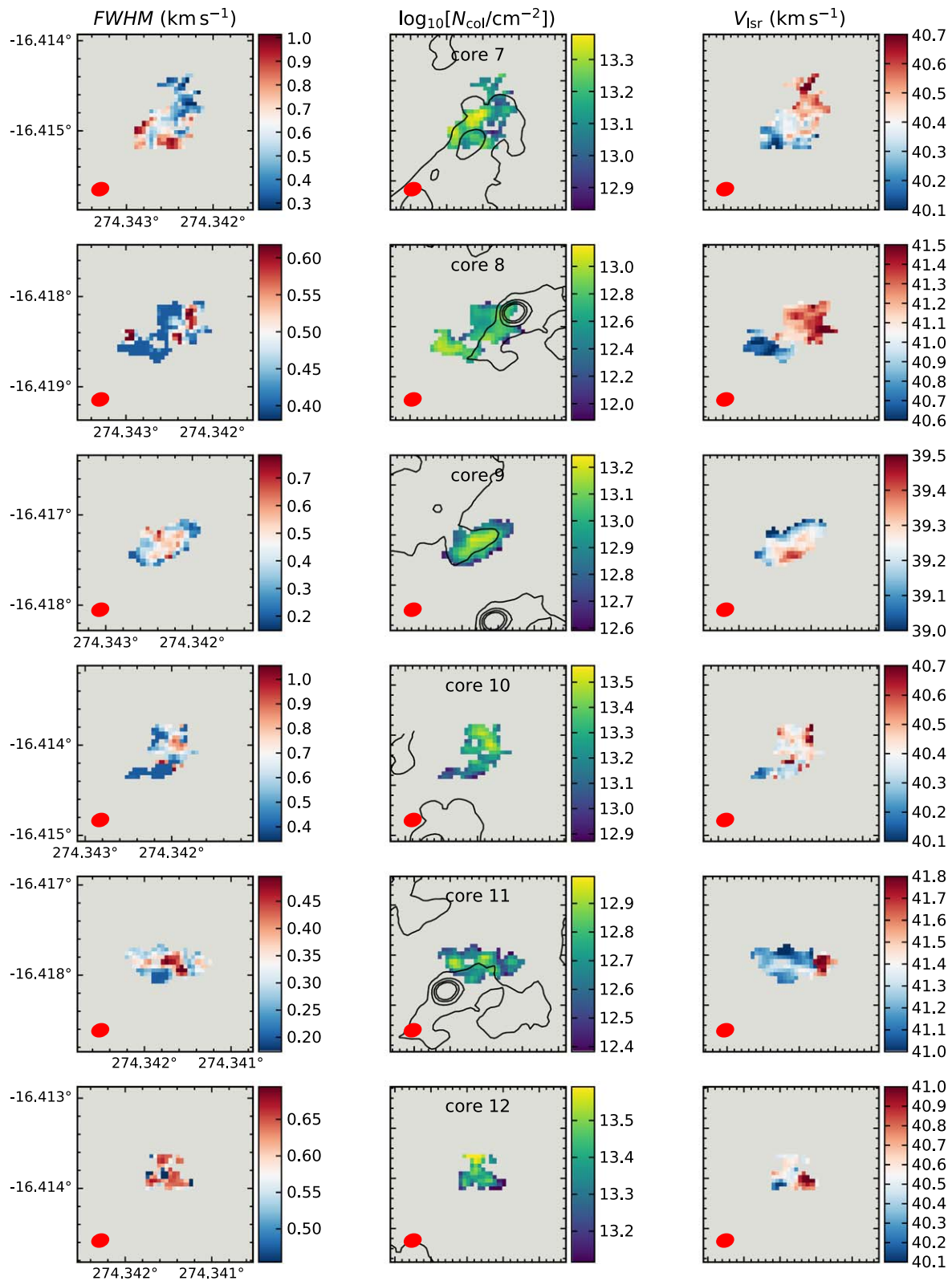


Figure B2. Continuation of Figure B1.

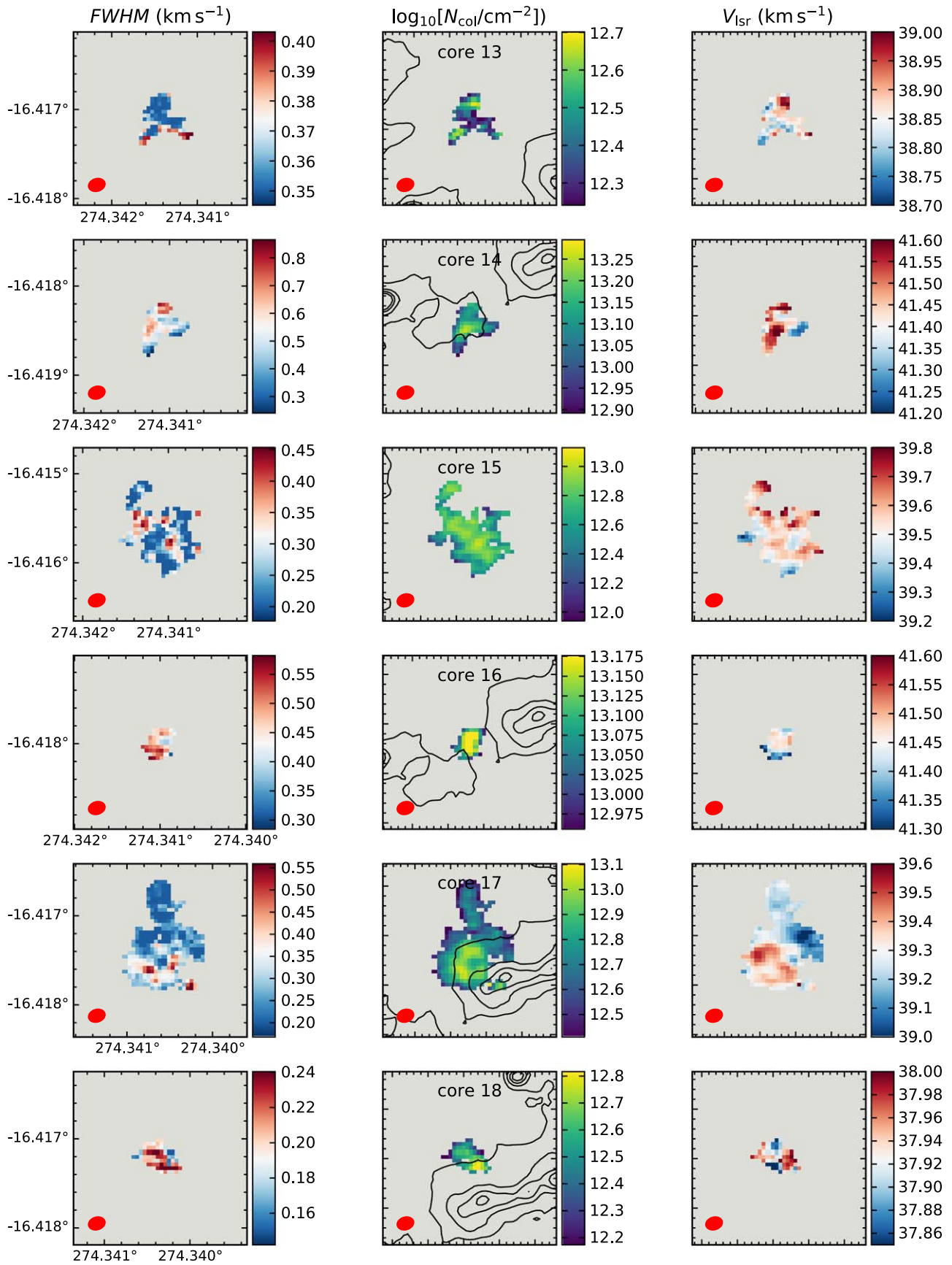


Figure B3. Continuation of Figure B1.

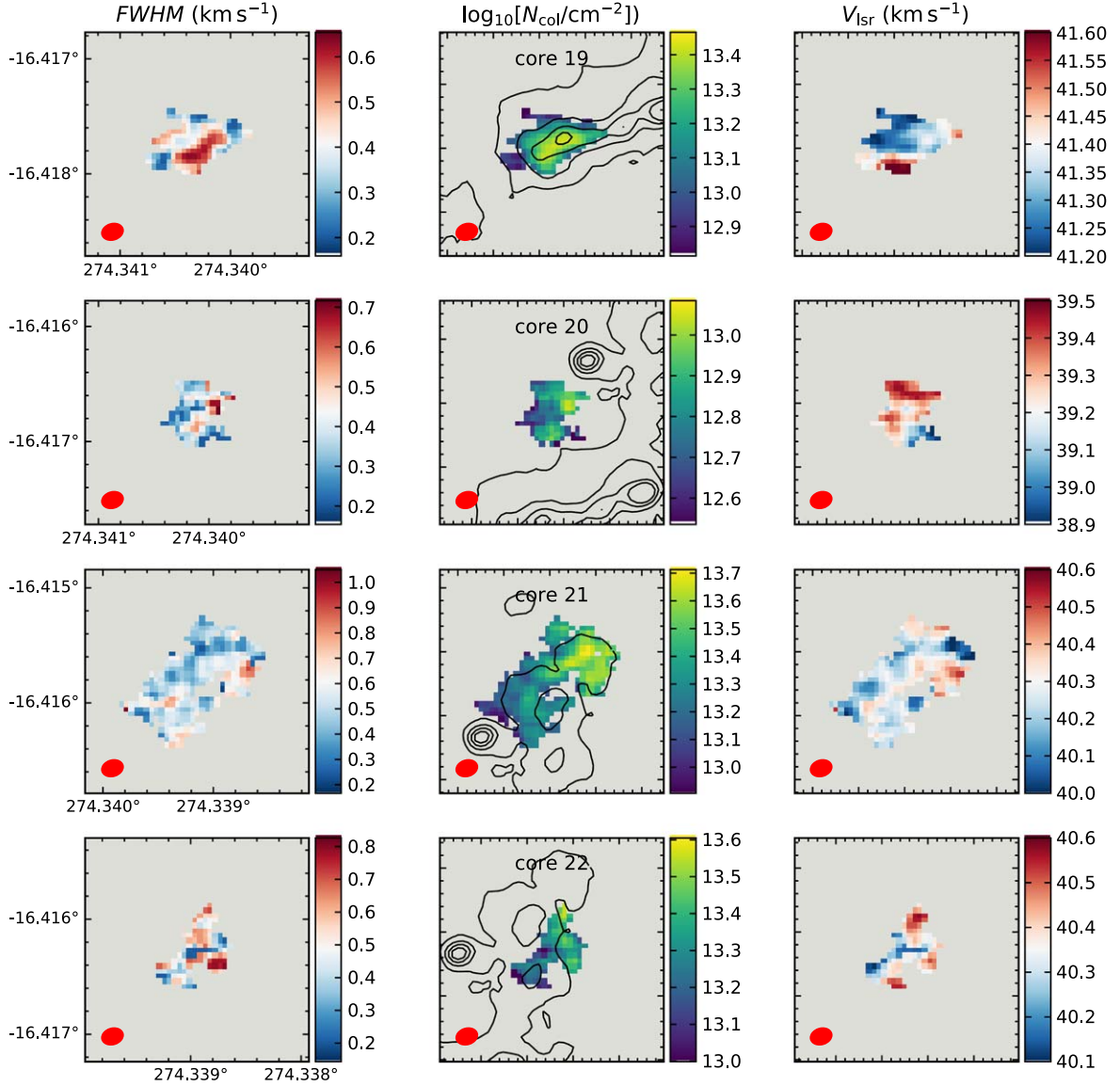


Figure B4. Continuation of Figure B1.

Appendix C

Opacity and Missing Flux of the o-H₂D⁺(1_{1,0}-1_{1,1}) Line

In order to estimate the opacity of the o-H₂D⁺(1_{1,0}-1_{1,1}) line, we make use of the equation:

$$\tau_\nu = -\ln \left[1 - \frac{T_b}{J_\nu(T_{\text{ex}}) - J_\nu(T_{\text{bg}})} \right], \quad (\text{C1})$$

where $J_\nu(T)$ is the equivalent Rayleigh–Jeans temperature at the frequency ν and temperature T , and $T_{\text{bg}} = 2.73$ K is the background temperature. In the ALMA data, the brightness temperature peaks at 2 K. Using $T_{\text{ex}} = 10$ K, Equation (C1) yields $\tau_\nu \approx 0.8$. Even in the brightest part of the emission, hence, the line is only moderately optically thick. With this information, we can also estimate by how much the line widths would be overestimated toward the positions of the source with the highest optical depth. To do so, we make use of Equation

(52) of Burton et al. (1992):

$$\sigma_{\text{obs}} = \frac{\sigma_0}{\sqrt{\ln(2)}} \left\{ \ln \left[\frac{\tau_\nu}{\ln \left(\frac{2}{1 + e^{-\tau_\nu}} \right)} \right] \right\}^{\frac{1}{2}}, \quad (\text{C2})$$

which allows to infer the observed velocity dispersion σ_{obs} from the intrinsic one σ_0 given the line opacity τ_ν . Using the maximum value for the opacity just found, we estimate that in the most optically thick parts of the source the o-H₂D⁺(1_{1,0}-1_{1,1}) line width is overestimated by 15%.

The ALMA Band 7 data lack of Total Power observations, which is crucial for recovering the large-scale emission from the source. In order to quantify if and how the observations are affected by filtering-out, we compare the o-H₂D⁺(1_{1,0}-1_{1,1}) spectra observed with the APEX single-dish telescope toward AG14 (Sabatini et al. 2020) with the ALMA data in Figure C1.

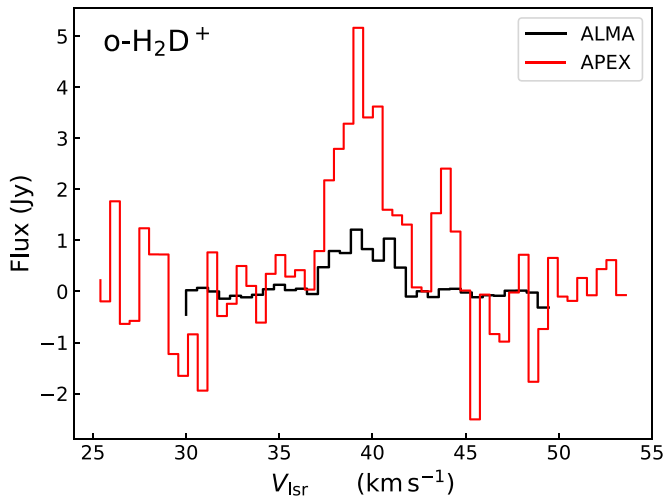


Figure C1. Comparison of the $\text{o-H}_2\text{D}^+(1_{1,0}-1_{1,1})$ spectra obtained toward AG14 with the APEX single-dish telescope (red histogram) and the ALMA interferometer (black histogram). See the text for the technical details about how the spectra were extracted.

The APEX data have been converted in flux unit using the gain¹⁶ $G_{\text{APEX}} = 40 \text{ Jy K}^{-1}$. The ALMA data instead have been integrated over an area equal to the beam size of the single-dish ($\theta_{\text{APEX}} = 16''.8$) and smoothed to the same spectral resolution.

Figure C1 shows that the interferometer is recovering only \sim one fifth of the emission. The missing flux arises from the large scales, as the emission is more extended than the maximum recoverable scale of the telescope in this configuration ($\theta_{\text{MRS}} \approx 20''$, as was already noted for AG351 and AG354 in Redaelli et al. 2021). However, the ALMA data do not usually present anomalous line shapes. Furthermore, the core identified by SCIMES are significantly smaller than $\theta_{\text{MRS}} \approx 20''$. We hence conclude that the missing flux problem does not affect significantly the analysis of the present work.

Appendix D

N_2H^+ Fitting and Full Results of ACORNS Clustering

The multicomponent Gaussian fit of the N_2H^+ isolated hyperfine transition, performed with the PYSPECKIT package, has nine free parameters in total: V_{lsr} , σ_v , and T_{peak} values, times three Gaussian components. To improve the code convergence, we first masked pixels with $S/N < 10$ in peak intensity. This choice leaves 5387 positions (55% of the total) unmasked, which however still cover the whole $\text{o-H}_2\text{D}^+$ FoV. We limited the space of the parameters as follows: $V_{\text{lsr}} \in [36; 43] \text{ km s}^{-1}$; $T_{\text{peak}} > 0 \text{ K}$; $\sigma_v \in [0; 2.5] \text{ km s}^{-1}$. Due to the large gradients of the free parameters over the map, the fitting routine does not converge everywhere. After a first procedure, we hence selected the spectra with residuals $> 2\sigma$ ($1\sigma = 120 \text{ mK}$; the rms of the residuals is computed in the velocity range $[34.6; 43.5] \text{ km s}^{-1}$), and we performed a second fit, adjusting the initial guesses on the free parameters. We checked the residuals after this second fitting routine, and their rms is found to be $< 3\sigma$. We further masked pixel-per-pixel

velocity components for which the fit did not converge, or with large uncertainties (e.g., $\sigma_{T_{\text{peak}}} > \text{K}$).

The best-fit results of the Gaussian fitting routine are fed to the clustering algorithm ACORNS. Unlike other similar codes, ACORNS uses the spectra line width as a further parameter to build the cluster hierarchy, and it is overall able to distinguish structures overlapping in the ppv space better than other algorithms, which becomes helpful for the crowded kinematics of AG14 (see also Appendix B in Henshaw et al. (2019) for further details on the comparison between different algorithms). We select the following clustering criteria in ACORNS:

1. Clusters must have a minimum size of 1.5 ALMA beam (to ensure that all the structures found are marginally resolved);
2. They must be separated in velocity less than the spectral resolution of the data cube;
3. The maximum separation in velocity dispersion (FWHM) is less than the gas thermal velocity at 10 K (0.19 km s^{-1});
4. The minimum height of an independent cluster is 3σ , and the stop criterion is set to 5σ ($1\sigma = 0.12 \text{ K}$).

After a first run, the code performs a second cycle of clustering, when we relax the criteria by 30%, which further helps building the hierarchical structure according to the prescriptions of ACORNS. At the end, the algorithm is able to cluster 87% of the data points, and it finds 18 trees, shown in Figure D1 as a dendrogram, and in Figure D2 in the ppv space. The large majority (more than 70%) of clustered data points belong to only four structures, which also contain $\approx 80\%$ of the total flux (A, B, C, and G as labeled in Figure D1). The remaining clusters contain less than 3% of the data points each. The analysis of Section 3.2 hence focuses on these four trees.

We now discuss why we prefer to use distinct software to analyze the N_2H^+ and $\text{o-H}_2\text{D}^+$ data. SCIMES is optimized to work with low-to-medium S/N data, such as the $\text{o-H}_2\text{D}^+$ ones. Furthermore, using it ensures a proper comparison with the results of Redaelli et al. (2021), which in turn allows us to obtain a larger sample, for instance, regarding the core masses. ACORNS, on the other hand, represents a better choice for analyzing the N_2H^+ data, first of all because it has less problems to disentangle crowded spectra such as the ones in AG14. SCIMES in fact works on the observed ppv data cubes, and it performs better when the multiple velocity components are well separated in the velocity space, as in the $\text{o-H}_2\text{D}^+$ data, where these components are separated by $\approx 1 \text{ km s}^{-1}$ and they are narrow ($\sigma_v = 0.3 \text{ km s}^{-1}$). On the contrary, the N_2H^+ spectra are more crowded, with more velocity components, and some of these components have significantly broader lines ($\sigma_v = 0.6\text{--}1.0 \text{ km s}^{-1}$). Due to these features, SCIMES is not able to disentangle them, as demonstrated by a test run of the software that we performed on the N_2H^+ data cube. ACORNS instead is able to perform this task because it works on decomposed data. There is also another important difference, in that ACORNS performs the clustering also in velocity dispersion space. The $\text{o-H}_2\text{D}^+(1_{1,0}-1_{1,1})$ line widths span a much smaller range ($\approx 0.2\text{--}0.4 \text{ km s}^{-1}$) with respect to the N_2H^+ ones ($\approx 0.3\text{--}1.5 \text{ km s}^{-1}$), and therefore this extra constraint helps even more in disentangling the N_2H^+ complex kinematics.

¹⁶ Listed at <http://www.apex-telescope.org/telescope/efficiency/>.

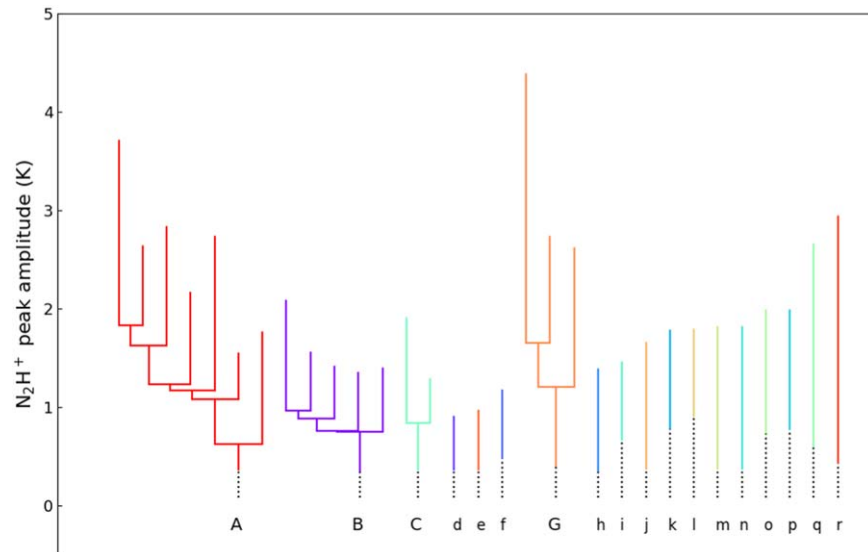


Figure D1. Results of the ACORNS clustering algorithm run on the results of the multicomponent Gaussian fitting of the N_2H^+ (1–0) transition, shown graphically as a dendrogram. The different colors represent distinct trees, labeled with letters, and they correspond to the structures shown in Figure D2. The four trees labeled with capital letters contain more than 70% of all data and 80% of the total flux.

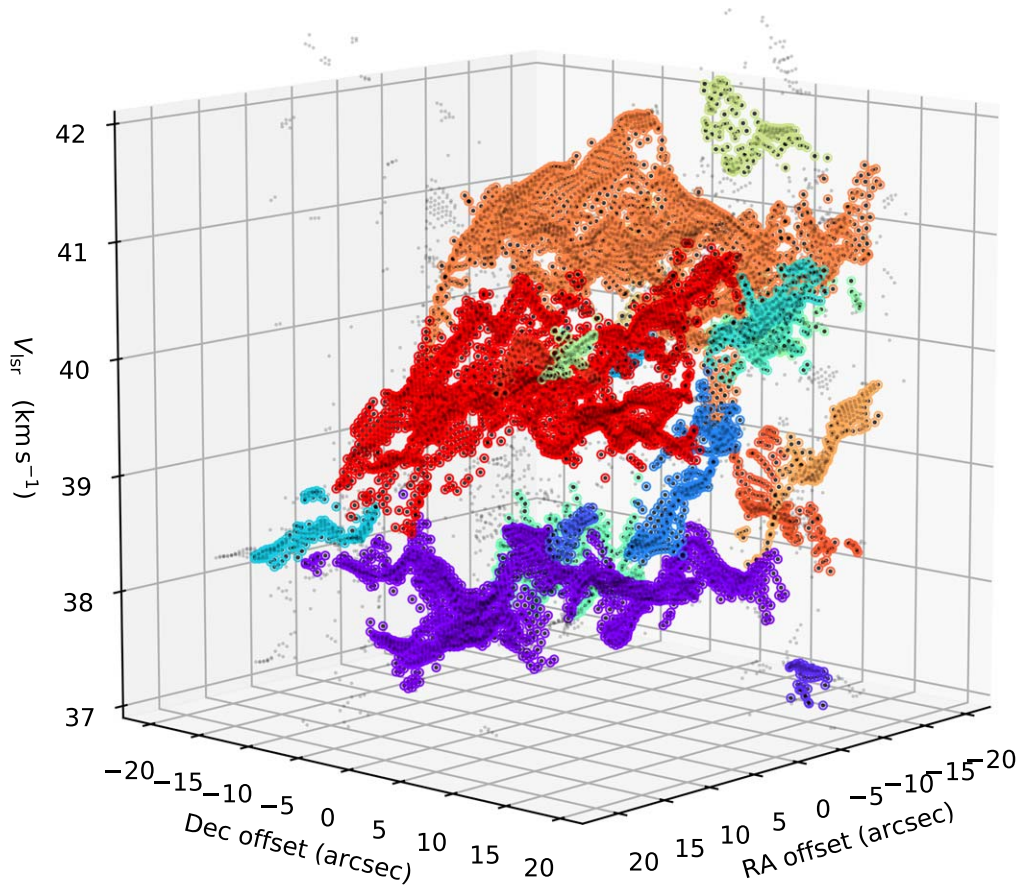

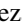





Figure D2. Ppv diagram with the complete set of trees identified by ACORNS. The coordinates axes are expressed as offsets (in arcsec) with respect to the position R.A. = $18^{\text{h}}17^{\text{m}}22^{\text{s}}.0$, decl. = $-16^{\circ}25'01''.7$. Each color represent a different tree, and have correspondence in the dendrogram shown in Figure D1. Gray points do not belong to any cluster.

ORCID iDs

Elena Redaelli  <https://orcid.org/0000-0002-0528-8125>
 Stefano Bovino  <https://orcid.org/0000-0003-2814-6688>
 Patricio Sanhueza  <https://orcid.org/0000-0002-7125-7685>
 Kaho Morii  <https://orcid.org/0000-0002-6752-6061>
 Giovanni Sabatini  <https://orcid.org/0000-0002-6428-9806>
 Paola Caselli  <https://orcid.org/0000-0003-1481-7911>
 Shanghuo Li  <https://orcid.org/0000-0003-1275-5251>

References

- Arzoumanian, D., André, P., Didelon, P., et al. 2011, *A&A*, **529**, L6
 Arzoumanian, D., André, P., Könyves, V., et al. 2019, *A&A*, **621**, A42
 Bacmann, A., Lefloch, B., Ceccarelli, C., et al. 2002, *A&A*, **389**, L6
 Baldeschi, A., Elia, D., Molinari, S., et al. 2017, *MNRAS*, **466**, 3682
 Barnes, A. T., Henshaw, J. D., Caselli, P., et al. 2018, *MNRAS*, **475**, 5268
 Beckwith, S. V. W., Sargent, A. I., Chini, R. S., & Guesten, R. 1990, *AJ*, **99**, 924
 Bertoldi, F., & McKee, C. F. 1992, *ApJ*, **395**, 140
 Bonnell, I. A., & Bate, M. R. 2006, *MNRAS*, **370**, 488
 Bonnell, I. A., Bate, M. R., Clarke, C. J., & Pringle, J. E. 2001, *MNRAS*, **323**, 785
 Burton, W. B., Elmegreen, B. G., Genzel, R., et al. 1992, Saas-Fee Advanced Course 21: The Galactic Interstellar Medium (Heidelberg: Springer Berlin)
 Caselli, P., Vastel, C., Ceccarelli, C., et al. 2008, *A&A*, **492**, 703
 Caselli, P., Walmsley, C. M., Tafalla, M., Dore, L., & Myers, P. C. 1999, *ApJ*, **523**, L165
 Ceccarelli, C., Caselli, P., Bockelée-Morvan, D., et al. 2014, in Protostars and Planets VI, ed. H. Beuther et al. (Tucson, AZ: Univ. Arizona Press), 859
 Chen, H.-R. V., Zhang, Q., Wright, M. C. H., et al. 2019, *ApJ*, **875**, 24
 Colombo, D., Rosolowsky, E., Ginsburg, A., Duarte-Cabral, A., & Hughes, A. 2015, *MNRAS*, **454**, 2067
 Contreras, Y., Sanhueza, P., Jackson, J. M., et al. 2018, *ApJ*, **861**, 14
 Cornwell, T. J. 2008, *ISTSP*, **2**, 793
 Fontani, F., Barnes, A. T., Caselli, P., et al. 2021, *MNRAS*, **503**, 4320
 Friesen, R. K., Di Francesco, J., Bourke, T. L., et al. 2014, *ApJ*, **797**, 27
 Giannetti, A., Leurini, S., Wyrowski, F., et al. 2017, *A&A*, **603**, A33
 Giannetti, A., Wyrowski, F., Brand, J., et al. 2014, *A&A*, **570**, A65
 Giannetti, A., Bovino, S., Caselli, P., et al. 2019, *A&A*, **621**, L7
 Ginsburg, A., & Mirocha, J. 2011, PySpecKit: Python Spectroscopic Toolkit, Astrophysics Source Code Library, ascl:1109.001
 Goldsmith, P. F. 2001, *ApJ*, **557**, 736
 Guzmán, A. E., Sanhueza, P., Contreras, Y., et al. 2015, *ApJ*, **815**, 130
 Hacar, A., Clark, S., Heitsch, F., et al. 2022, arXiv:2203.09562
 Henshaw, J. D., Caselli, P., Fontani, F., Jiménez-Serra, I., & Tan, J. C. 2014, *MNRAS*, **440**, 2860
 Henshaw, J. D., Ginsburg, A., Haworth, T. J., et al. 2019, *MNRAS*, **485**, 2457
 Hildebrand, R. H. 1983, *QJRAS*, **24**, 267
 Hugo, E., Asvany, O., & Schlemmer, S. 2009, *JChPh*, **130**, 164302
 Jusko, P., Töpfer, M., Müller, H. S. P., et al. 2017, *JMoSp*, **332**, 33
 Kauffmann, J., Bertoldi, F., Bourke, T. L., Evans, N. J. I., & Lee, C. W. 2008, *A&A*, **487**, 993
 Kauffmann, J., & Pillai, T. 2010, *ApJL*, **723**, L7
 Kauffmann, J., Pillai, T., & Goldsmith, P. F. 2013, *ApJ*, **779**, 185
 Köngig, C., Urquhart, J. S., Csengeri, T., et al. 2017, *A&A*, **599**, A139
 Krumholz, M. R., & McKee, C. F. 2008, *Natur*, **451**, 1082
 Kuiper, R., Turner, N. J., & Yorke, H. W. 2016, *ApJ*, **832**, 40
 Li, S., Zhang, Q., Pillai, T., et al. 2019, *ApJ*, **886**, 130
 Li, S., Zhang, Q., Liu, H. B., et al. 2020, *ApJ*, **896**, 110
 Li, S., Sanhueza, P., Zhang, Q., et al. 2020, *ApJ*, **903**, 119
 Li, S., Sanhueza, P., Lee, C. W., et al. 2022, *ApJ*, **926**, 165
 Lu, X., Zhang, Q., Liu, H. B., et al. 2018, *ApJ*, **855**, 9
 MacLaren, I., Richardson, K. M., & Wolfendale, A. W. 1988, *ApJ*, **333**, 821
 Maret, S., Hily-Blant, P., Pety, J., Bardeau, S., & Reynier, E. 2011, *A&A*, **526**, A47
 McKee, C. F., & Tan, J. C. 2003, *ApJ*, **585**, 850
 McMullin, J. P., Waters, B., Schiebel, D., Young, W., & Golap, K. 2007, in ASP Conf. Ser. 376, Astronomical Data Analysis Software and Systems XVI, ed. R. A. Shaw, F. Hill, & D. J. Bell (San Francisco, CA: ASP), 127
 Mezger, P. G., Wink, J. E., & Zylka, R. 1990, *A&A*, **228**, 95
 Morii, K., Sanhueza, P., Nakamura, F., et al. 2021, *ApJ*, **923**, 147
 Myers, P. C., Ladd, E. F., & Fuller, G. A. 1991, *ApJL*, **372**, L95
 Ohashi, S., Sanhueza, P., Chen, H.-R. V., et al. 2016, *ApJ*, **833**, 209
 Ostriker, J. 1964, *ApJ*, **140**, 1056
 Palmeirim, P., André, P., Kirk, J., et al. 2013, *A&A*, **550**, A38
 Patil, A., Huard, D., & Fomesbeck, C. J. 2010, *J. Stat. Softw.*, **35**, 1
 Peretto, N., Fuller, G. A., André, P., et al. 2014, *A&A*, **561**, A83
 Pillai, T., Kauffmann, J., Zhang, Q., et al. 2019, *A&A*, **622**, A54
 Pon, A., Toalá, J. A., Johnstone, D., et al. 2012, *ApJ*, **756**, 145
 Rathborne, J. M., Jackson, J. M., & Simon, R. 2006, *ApJ*, **641**, 389
 Redaelli, E., Bovino, S., Giannetti, A., et al. 2021, *A&A*, **650**, A202
 Rosolowsky, E., & Leroy, A. 2006, *PASP*, **118**, 590
 Rosolowsky, E. W., Pineda, J. E., Kauffmann, J., & Goodman, A. A. 2008, *ApJ*, **679**, 1338
 Sabatini, G., Giannetti, A., Bovino, S., et al. 2019, *MNRAS*, **490**, 4489
 Sabatini, G., Bovino, S., Giannetti, A., et al. 2020, *A&A*, **644**, A34
 Sabatini, G., Bovino, S., Sanhueza, P., et al. 2022, *ApJ*, **936**, 80
 Sakai, T., Sanhueza, P., Furuya, K., et al. 2022, *ApJ*, **925**, 141
 Sanhueza, P., Jackson, J. M., Foster, J. B., et al. 2012, *ApJ*, **756**, 60
 Sanhueza, P., Jackson, J. M., Foster, J. B., et al. 2013, *ApJ*, **773**, 123
 Sanhueza, P., Jackson, J. M., Zhang, Q., et al. 2017, *ApJ*, **841**, 97
 Sanhueza, P., Contreras, Y., Wu, B., et al. 2019, *ApJ*, **886**, 102
 Sanhueza, P., Girart, J. M., Padovani, M., et al. 2021, *ApJL*, **915**, L10
 Singh, A., Matzner, C. D., Friesen, R. K., et al. 2021, *ApJ*, **922**, 87
 Sipilä, O., Caselli, P., & Harju, J. 2013, *A&A*, **554**, A92
 Sipilä, O., Caselli, P., & Harju, J. 2015, *A&A*, **578**, A55
 Smith, R. J., Longmore, S., & Bonnell, I. 2009, *MNRAS*, **400**, 1775
 Sokolov, V., Wang, K., Pineda, J. E., et al. 2019, *ApJ*, **872**, 30
 Svoboda, B. E., Shirley, Y. L., Traficante, A., et al. 2019, *ApJ*, **886**, 36
 Tafoya, D., Sanhueza, P., Zhang, Q., et al. 2021, *ApJ*, **925**, 141
 Tan, J. C., Beltrán, M. T., Caselli, P., et al. 2014, Protostars and Planets VI (Tucson, AZ: Univ. Arizona Press), 149
 Tan, J. C., Kong, S., Butler, M. J., Caselli, P., & Fontani, F. 2013, *ApJ*, **779**, 96
 Tan, J. C., Kong, S., Zhang, Y., et al. 2016, *ApJL*, **821**, L3
 Toalá, J. A., Vázquez-Semadeni, E., & Gómez, G. C. 2012, *ApJ*, **744**, 190
 Walker, C. K., Adams, F. C., & Lada, C. J. 1990, *ApJ*, **349**, 515
 Wang, J.-W., Koch, P. M., Galván-Madrid, R., et al. 2020, *ApJ*, **905**, 158
 Wang, P., Li, Z.-Y., Abel, T., & Nakamura, F. 2010, *ApJ*, **709**, 27
 Williams, G. M., Peretto, N., Avison, A., Duarte-Cabral, A., & Fuller, G. A. 2018, *A&A*, **613**, A11
 Zhang, Q., Wang, K., Lu, X., & Jiménez-Serra, I. 2015, *ApJ*, **804**, 141